remote sensing

MDPI

Article

Combining Multispectral and Radar Imagery with Machine Learning Techniques to Map Intertidal Habitats for Migratory Shorebirds

Mohamed Henriques [1,2,*], Teresa Catry [1], João Ricardo Belo [1,2,3], Theunis Piersma [2,4], Samuel Pontes [5] and José Pedro Granadeiro [1]

1 Center for Environmental and Marine Studies (CESAM), Department of Animal Biology, Faculty of Sciences, University of Lisbon, 1749-016 Lisbon, Portugal; tcatry@fc.ul.pt (T.C.); jrbelo@ua.pt (J.R.B.); jpgranadeiro@fc.ul.pt (J.P.G.)
2 Conservation Ecology Group, Groningen Institute for Evolutionary Life Sciences, University of Groningen, 9700 CC Groningen, The Netherlands; theunis.piersma@nioz.nl
3 Center for Environmental and Marine Studies (CESAM), Department of Biology, University of Aveiro, 3810-193 Aveiro, Portugal
4 Department of Coastal Systems, NIOZ-Royal Netherlands Institute for Sea Research, 1797 SZ Texel, The Netherlands
5 Instituto da Biodiversidade e Áreas Protegidas Dr. Alfredo Simão da Silva-IBAP, Bissau, Guinea-Bissau; saemmalepon@gmail.com
* Correspondence: mhenriquesbalde@gmail.com; Tel.: +351-217-500-000 (ext. 22607)

Abstract: Migratory shorebirds are notable consumers of benthic invertebrates on intertidal sediments. The distribution and abundance of shorebirds will strongly depend on their prey and on landscape and sediment features such as mud and surface water content, topography, and the presence of ecosystem engineers. An understanding of shorebird distribution and ecology thus requires knowledge of the various habitat types which may be distinguished in intertidal areas. Here, we combine Sentinel-1 and Sentinel-2 imagery and a digital elevation model (DEM), using machine learning techniques to map intertidal habitat types of importance to migratory shorebirds and their benthic prey. We do this on the third most important non-breeding area for migratory shorebirds in the East Atlantic Flyway, in the Bijagós Archipelago in West Africa. Using pixel-level random forests, we successfully mapped rocks, shell beds, and macroalgae and distinguished between areas of bare sediment and areas occupied by fiddler crabs, an ecosystem engineer that promotes significant bioturbation on intertidal flats. We also classified two sediment types (sandy and mixed) within the bare sediment and fiddler crab areas, according to their mud content. The overall classification accuracy was 82%, and the Kappa Coefficient was 73%. The most important predictors were elevation, the Sentinel-2-derived water and moisture indexes, and Sentinel-1 VH band. The association of Sentinel-2 with Sentinel-1 and a DEM produced the best results compared to the models without these variables. This map provides an overall picture of the composition of the intertidal habitats in a site of international importance for migratory shorebirds. Most of the intertidal flats of the Bijagós Archipelago are covered by bare sandy sediments (59%), and ca. 22% is occupied by fiddler crabs. This likely has significant implications for the spatial arrangement of the shorebird and benthic invertebrate communities due to the ecosystem engineering by the fiddler crabs, which promotes two vastly different intertidal species assemblages. This large-scale mapping provides an important product for the future monitoring of this high biodiversity area, particularly for ecological research related to the distribution and feeding ecology of the shorebirds and their prey. Such information is key from a conservation and management perspective. By delivering a successful and comprehensive mapping workflow, we contribute to the filling of the current knowledge gap on the application of remote sensing and machine learning techniques within intertidal areas, which are among the most challenging environments to map using remote sensing techniques.

Citation: Henriques, M.; Catry, T.; Belo, J.R.; Piersma, T.; Pontes, S.; Granadeiro, J.P. Combining Multispectral and Radar Imagery with Machine Learning Techniques to Map Intertidal Habitats for Migratory Shorebirds. *Remote Sens.* **2022**, *14*, 3260. https://doi.org/10.3390/rs14143260

Academic Editor: Aaron Moody

Received: 16 May 2022
Accepted: 3 July 2022
Published: 6 July 2022

Keywords: intertidal flats; Sentinel-1; Sentinel-2; remote sensing; intertidal sediments; random forest

1. Introduction

Intertidal flats constitute complex transitional systems occurring in the interface between the sea and land. They are estimated to cover at least 127,921 km^2 [1] and include a variety of important habitat types, such as rocky reefs, shell beds, seagrass and macroalgae mats, and soft exposed sediments [2]. Intertidal flats support high biodiversity levels and complex benthic food webs [3], including high-level consumers such as migratory shorebirds, which play an important role in structuring processes in intertidal food webs [4,5]. These birds depend entirely on intertidal areas for foraging during their non-breeding periods [6], where they congregate at low tide to feed on benthic invertebrate prey [7]. Alarmingly, intertidal areas are declining at an unprecedented rate [1], and shorebirds are experiencing widespread population declines [8,9], including in the East Atlantic Flyway (EAF; [10,11]. The causes for these flyway-wide declines are mostly unknown, with insights only for two well-studied species, Bar-tailed godwits *Limosa lapponica* and Red Knots *Calidris canutus*, both linked to a reduction in fitness observed in non-breeding areas but caused by global warming effects on breeding sites [12,13].

Among the main non-breeding sites along the EAF, the Bijagós Archipelago in Guinea-Bissau (West Africa) stands as the third most important area for migratory shorebirds, annually sustaining hundreds of thousands of birds coming from their northern European and Arctic breeding sites [14,15]. However, as in other sites within the flyway, very steep declines in the populations of several shorebird species have been occurring in the Bijagós Archipelago [16]. Understanding these declines is important in order to expand our knowledge of the extent and the spatial arrangement of intertidal habitats of relevance to shorebirds, especially with regard to their benthic invertebrate prey [17]; to provide the necessary tools to further monitor the impact of ongoing and future changes; and to deepen our understanding of species–habitat relationships.

The occurrence, behaviour, and abundance of benthic invertebrate prey in intertidal sediments depends largely on the landscape and sediment characteristics, such as mud and surface water content [18], grain size [19], and elevation [20]. The presence of ecosystem engineers in intertidal flats may also influence the biotic and abiotic components of the ecosystem [21], affecting the benthic invertebrates and shorebirds, as is the case with macroalgae [22] and fiddler crabs [23–25]. Thus, mapping the distribution of different intertidal sediment types and of these ecosystem engineers in intertidal ecosystems is also essential to better understand the distribution, foraging ecology, and habitat requirements of migratory shorebirds in key non-breeding sites (review in [26]).

Applying remote sensing to ecology has become a popular and efficient way to study and characterize the vast and often disjunct intertidal areas that would otherwise be extremely difficult to study and to allow the development of reliable maps of habitats with reduced costs and effort. There are several recent published records aiming at mapping the distribution of intertidal vegetation (e.g., [27–29], sediment types (e.g., [30–32], and benthic invertebrate beds [33–35]. Some studies have also focused on mapping intertidal areas as habitats for shorebirds, but most were solely focused on intertidal vegetation (e.g., [36,37] or were dedicated to breeding areas [35,38–40]. The lack of attention to non-breeding areas along the EAF highlights a significant knowledge gap regarding the distribution and extent of the different intertidal habitats on which shorebirds depend; this is particularly so in tropical regions, which are chronically less studied and understood.

The joint use of multispectral imagery and synthetic aperture radar (SAR) products has shown a great potential to advance our knowledge on the structure of ecosystems at large scales, to increase the opportunities to acquire spatially explicit data on species composition and distribution, and to map key habitat features [41]. Among several satellite constellations, the imagery made freely available by the Copernicus Program through

Sentinel-1 and Sentinel-2 missions [42] has significantly increased the potential to monitor ecosystems and detect and predict changes by featuring a higher spatial resolution and shorter revisitation cycle, in comparison to Landsat satellites, including multispectral and SAR products.

The mapping of intertidal flats can be very challenging due to the similarities between the spectral signatures of different habitat types, especially among areas with distinct sediment properties, which occur along smooth gradients and present subtle differences in their surface characteristics. Furthermore, as intertidal areas are subject to cyclical inundation periods, the spectral characteristics of the sediments can change substantially due to the presence of surface water [43,44]. Therefore, land cover classification exercises in intertidal areas require constant updates, allowing for the application of the latest advances in machine learning to deliver the best possible predictions. Among the most used machine learning algorithms, random forests [45] have been favoured by many recent studies focusing on supervised land cover classifications because of their flexibility, high accuracy, and computation efficiency in large datasets [46,47]. This has been further improved with the introduction of several variable selection algorithms, which reduce the number of variables (and therefore, reduce redundancy), and increase computation efficiency, classification accuracy, and the interpretability of the results [48]. Despite the multiple refined remote sensing methods currently available, there is still a lack of applied studies gathering the most suitable techniques in automated/semi-automated workflows aiming at classifying intertidal habitats.

By using well-established remote sensing and machine learning techniques, we aim to map, for the first time, the intertidal habitats of relevance to shorebirds and their benthic invertebrate prey in a key non-breeding area of the EAF of the Bijagós Archipelago. We combined data acquired by active (SAR) and passive (multispectral) sensors and a digital elevation model (DEM). We base this exercise on a thorough collection of the information in the field, which was used independently to train and validate classification algorithms. The workflow proposed includes a field reference data collection, satellite data collection and processing, computation of a DEM, variable selection, model training with random forest, and the application of a post-classification filter to produce the final output. Additionally, we assessed the benefits of combining multispectral, SAR, and DEM predictors to map intertidal habitat types by comparing our best model against alternative models excluding radar and DEM layers. With this study, we aim to contribute to filling the current knowledge gap on the application of remote sensing and machine learning methods in habitat classification in intertidal flats, one of the most challenging environments to map using remote sensing techniques, by proposing a generalizable workflow. It is also our objective to contribute with a baseline knowledge that is critical for further studies focused on shorebird ecology, distribution, and habitat use at a landscape scale in this key intertidal area.

2. Materials and Methods

2.1. Study Area

This study is focused on the Bijagós Archipelago (11°14′N; 16°04′W), a deltaic group of 88 islands and islets located off the coast of Guinea-Bissau, West Africa (Figure 1). The tidal regime is semi-diurnal, with spring tides reaching 4.5 m [49]. Around the islands, there are vast intertidal flats [50,51], with an additional 524 km^2 estimated to be covered by dense mangrove forests [52]. The entire intertidal area of the country is among the top 30 largest in the world [1]. In the Bijagós Archipelago, the intertidal flats are mainly composed of fine and coarser sandy and mixed sediments [15,53], with sedimentary origins connected mainly to the contribution of two rivers, Corubal and Geba [51]. The climate is bi-seasonal, with a dry and a wet season spanning from November to April and from May to October, respectively. The archipelago holds a variety of natural habitats, and it has been classified as a Biosphere Reserve, an Important Bird Area, and a Ramsar site, in recognition of the value of its biodiversity and international importance for many waterbird species [49].

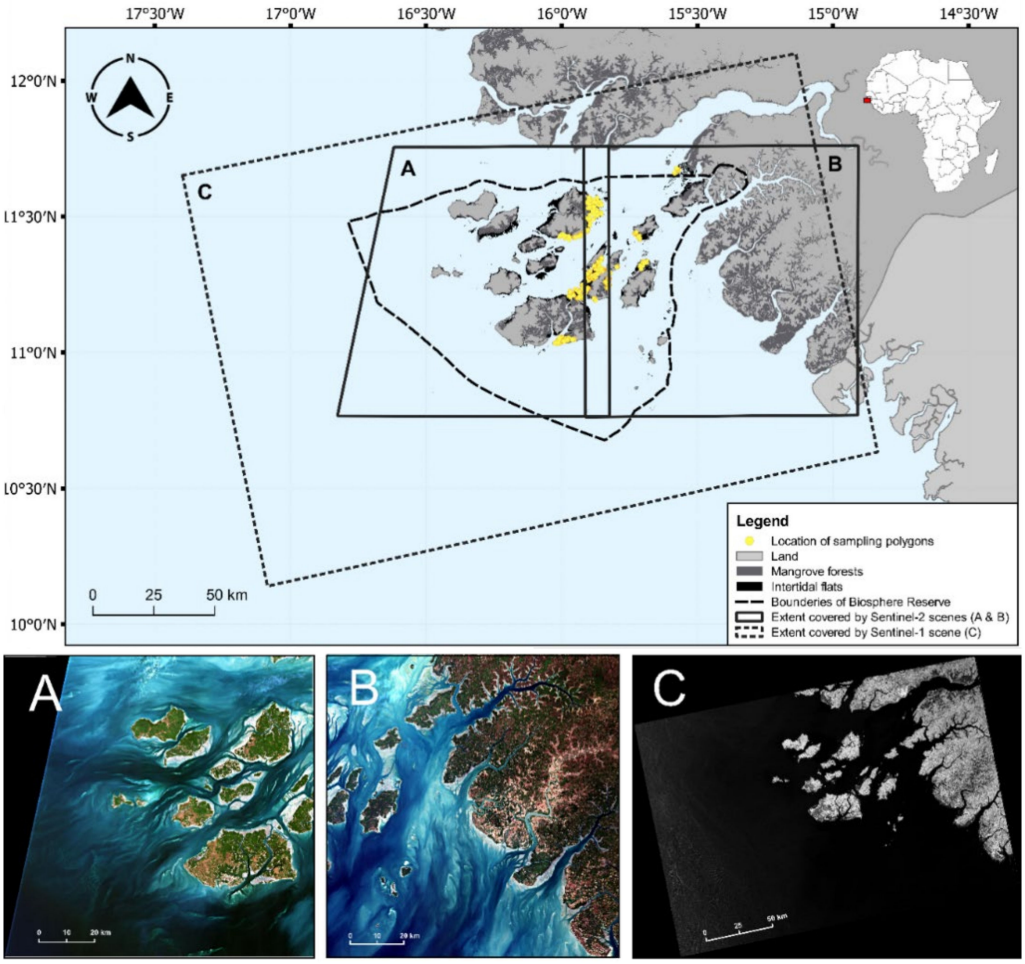

Figure 1. Map of study area, in the Bijagós Archipelago, showing the location of the sampling polygons used for field reference data collection, the limits of the Biosphere Reserve, and the extent covered by each satellite scene used in this study. (**A**,**B**) show RGB images of Sentinel-2 scenes using red, green, and blue bands; (**C**) shows a grey-scale RGB composite with two channels of Sentinel-1 VH and VV bands.

2.2. Overall Workflow

To classify the different intertidal habitat types, we combined individual bands and sets of band indexes derived from Sentinel-1 and Sentinel-2 imagery with a DEM, produced in this study from a time series of Sentinel-2 scenes representing different tidal stages, to use as potential predictors. Our workflow consisted of (1) an extensive collection of quantitative field reference data, including grain size analysis of sediment samples; (2) the defining of target shorebird intertidal habitats through a set of quantitative empirical thresholds; (3) the collecting and computing of a set of predictors from Sentinel-1 and Sentinel-2 imagery, including a Sentinel-2-derived DEM; (4) the employment of a modified recursive feature elimination algorithm to identify a minimal set of predictors; (5) the training of a random forest predictor with the selected predictors; (6) the validation of the quality of the final model against a fully independent dataset; (7) the production of a classification map for the entire study area; and (8) the employment of a post-classification filter to produce the final map. In addition, we assessed the benefits (in terms of classification accuracy) of combining data from different sensors by comparing the final model and the final map with models and maps produced by alternative models without Sentinel-1 and DEM layers.

2.3. Field Reference Data

We focused our field descriptors on the habitat properties known to influence foraging shorebirds and their prey, namely the mud content [54,55], the amount of hard material in the sediment (such as dead shells; [56], the presence of rocks [57], the macroalgae cover [58,59], and the presence of ecosystem engineers [21].

2.3.1. Field Sampling

The field reference data were collected from a large part of the study area during the dry season, in November 2019 and between February and March 2020. We selected 17 sampling areas, and within these, we randomly assigned a total of 170 sampling sites to ensure spatial and habitat variability (Figure 1). The sites were accessed by foot and by boat and several different areas (representing different sampling polygons) were sampled at each site within a ca. 500 m radius, to capture all visible heterogeneity. Therefore, the size of each polygon within the sampling sites was variable and designed to comprise uniform habitat units. This approach allowed us to collect data for a much larger area, compared to traditional pixel-by-pixel sampling. Within each polygon, we visually estimated the percentage cover by rocks, shells, macroalgae, water film, and the extent of the fiddler crab burrows. Areas with fiddler crab burrows typically only occur in very low or high densities and are visually very distinct (see [25]. Here, we only considered high density burrow areas, as described in [25]. Additionally, we collected 60 mL sediment samples within several polygons of different habitat types to conduct grain size analysis. When several polygons of the same habitat unit were sampled in the same sampling site, only one sediment sample was collected to represent these polygons.

2.3.2. Grain Size Analysis

The sediment samples were sun-dried in the field and stored in plastic containers for further processing. In the laboratory, the grains were disaggregated using a pestle and mortar and dried again at 50 °C for 24–48 h. We chose mud content (which represents the percentage weight of sediments <63 µm) as the defining variable to distinguish between different types of sediment. Each sample (averaging ca. 57 g) was weighted and then dry-sieved through a certified 63 µm mesh size sieve, separating sediment sizes >63 µm from the remaining sample, using an electric sieve shaker. The sediments retained in the sieve were then weighted (to the nearest 0.01 g) to obtain the proportion of mud content (fraction of sediments <63 µm) in relation to the whole sample. When a sample represented more than one polygon, the same values were attributed to all the related polygons.

2.4. Definition of Shorebird Intertidal Habitats

The habitat types were defined from the known shorebird preferences. The presence of structures covering the intertidal sediments can limit the access of shorebirds to their prey, by hindering their foraging efficiency (as is the case with macroalgae mats; [58] or by blocking access to the sediment altogether (rocks and shell beds), while it may also reduce the availability of their prey [56,58]. On the other hand, intertidal rocks, macroalgae mats, and ecosystem engineers such as fiddler crabs may play an important role in structuring shorebird and benthic invertebrate communities, offering conditions favoured by some species and avoided by others [23,25,57,60]. Moreover, both the shorebirds and their prey are widely known to show different preferences in relation to sediment mud content [54,61,62]. Taking this into account, the habitat types were defined using a combination of quantitative thresholds, based on the ground truthing variables and on the grain size analysis. The threshold limits for the ground truthing variables were decided based on two "rules of thumb": (1) areas covered by 30% or more of rocks, shells, or macroalgae were classified as belonging to those habitat types, otherwise they were classified as exposed sediment; (2) if exposed sediment areas were covered by more than 50% of high-density fiddler crab burrows, they were classified as fiddler crab burrow (FCB) areas, otherwise we considered them bare sediment areas. Within both the bare sediment and the FCB areas,

we then applied thresholds based on mud content to separate different sediment types. For this, we followed the class boundaries defined in [2]) (adapted from [63]), in which sandy areas are defined to have 10% or less of mud content, muddy sand features between 10–50%, sandy mud between 50–90%, and mud between 90–100%.

2.5. Satellite Imagery Selection and Processing

2.5.1. Selection of Satellite Images

To produce a water and land mask to extract the intertidal area, compute a DEM, and undertake the supervised classification of the intertidal habitats, we used the Sentinel-1 and Sentinel-2 satellite imagery freely available from the Copernicus Open Access Hub (https://scihub.copernicus.eu/; last accessed on 30 October 2021).

Sentinel-1 carries an active synthetic aperture radar (SAR) instrument that acquires images of the earth's surface by emitting C-band microwaves (at 5.405 GHz) and reading their backscattering reflections in dual-polarisation modes (vertical and horizontal waves). This allows this instrument to acquire images in all weather conditions, during the day and night. Sentinel-2 delivers a multispectral imaging of the earth's surface by passively reading the reflection of the sun light [64]. This limits the usability of these images only to daylight and according to cloud cover at the time of acquisition. Sentinel-2 samples 13 spectral bands: four bands at a 10 m × 10 m pixel spatial resolution (covering visible and near infrared regions), six bands at a 20 m resolution (red-edge and short-wave infrared regions), and three bands at a 60 m resolution (coastal aerosol, water vapor and cirrus). Further technical details can be found at https://sentinels.copernicus.eu/; accessed on 10 December 2021.

For the Sentinel-1 image, we used a Level-1 Ground Range Detected image acquired in the Interferometric Wide Swath mode, with a high geometric resolution (pixel size) of 5 m × 20 m, resampled to a pixel size of 10 m × 10 m. Sentinel-1 VH/VV dual-polarisation images were the only options available for our study area. For the Sentinel-2 images, we used Level-2A Bottom-of-Atmosphere reflectances acquired directly from Copernicus Open Access Hub. The Level 2A images were atmospherically corrected, using the algorithm ATCOR-2/3 [65]. Coastal aerosol, water vapor, and cirrus bands were not used in this study because they have no land use applications. Sentinel-1A had a revisitation period for our study area of 12 days, and the sensing time was at ca. 19h17. Sentinel-2 satellites revisited the study area every 5 days and acquired images between 11h21 and 11h23. For the supervised classifications, we chose a Sentinel-1A scene sensed on 28 January 2020 and two Sentinel-2A adjacent scenes (T28PCT and T28PDT, to cover the full extent of the study area), both from 4 February 2020, with less than 10% of cloud cover at the acquisition time. These dates are within (in the case of Sentinel-2A) or very close to (in the case of Sentinel-1A) the period of the collection of the field reference data. The sensing time captured the period closest to the low-tide peak. To produce the intertidal mask and the digital elevation model, we selected a time series of Sentinel-2 images covering as best as possible the ebbing and rising tide periods, resulting in 29 images for each of the two different scenes (T28PCT and T28PDT), from April 2019 to May 2021 (Table S1).

2.5.2. Sentinel-1 and Sentinel-2 Image Pre-Processing Methods

Sentinel-2 multispectral bands with primary resolutions of 20 m × 20 m pixels were resampled to 10 m to match the remaining high-resolution bands. To achieve this, we applied the nearest neighbour resampling method within the Sentinel Applications Platform (SNAP v. 8.0.8, Snap Inc., Santa Monica, CA, USA). Then, all the pre-processed bands were converted to true reflectance by dividing the digital numbers by the quantification number (10,000).

Sentinel-1 image pre-processing followed the workflow published in [66], which consisted of seven processing steps implemented through SNAP. The speckle noise reduction was conducted through the application of a Lee-Sigma filter [67]. Range Doppler terrain correction was made using the DEM produced in this study (for more details, consult [66–68].

2.5.3. Intercalibration of Sentinel-2 Scenes

The images from different dates of the Sentinel-2 time series may present discrepancies in their reflectance values because of different acquiring conditions among the days (see [69]). Likewise, the reflectance values of the two adjacent Sentinel-2 scenes that encompass the entire area of interest were not directly comparable, mainly because of the inherent differences in the reflection of light captured by the twin satellites, despite the fact that the acquisition times were virtually the same (Figure S1). Hence, we undertook an inter-date and inter-scene image calibration. Firstly, for the inter-date calibration, we intercalibrated the images from different dates, as described in Granadeiro et al., (2021), using the *lmodel2* package [70] in R to calculate a band-wise major axis regression between one reference image (any image can be selected) and all the other images. For the inter-scene calibration, we then used one reference scene (either of the two scenes can be selected as a reference) of each date of the time series and merged it with the adjacent scene. As the two adjacent Sentinel-2 scenes had an overlapping area (Figure 1), we extracted that region from both scenes and performed another major axis regression to rescale the reflectance values of the second scene to match the range of reflectance values of the reference scene (Figure S1). Thus, we obtained a final time series of larger Sentinel-2 images covering the whole study area by merging the adjacent intercalibrated scenes. The merging was performed by keeping the entire extension of the T28PCT scene and cropping out the overlapping area from the T28PDT.

2.5.4. Extraction of the Intertidal Area Water and Land Mask

We followed an established method, relying on a Sentinel-2 time series to identify and select the intertidal area to be classified [69,71,72]. We calculated the normalized difference water index (NDWI; [73]) for each image to enhance the contrast between the water and land pixels (NDWI is obtained from the green (Band 3) and the near-infrared (Band 8) bands). The concept behind this method is that permanent water bodies and land masses present relatively stable conditions (and show NDWI values with low temporal variance), whereas intertidal areas will have a higher variability in the NDWI values across the tidal time series of images as they are subject to cyclic inundation periods. A water and a land mask were then derived to be used in the subsequent steps of the methods, using the value of 0.2 as the variance threshold to identify intertidal areas (Figure S2; see [69,72]) for methodological details).

2.5.5. Digital Elevation Model and Final Study Area Extent

A DEM was derived from the time series of intercalibrated Sentinel-2 images following the method first described in Granadeiro et al., (2021), which includes the use of a modified logistic function and corrections of water height due to spatial differences in the tidal phase (hence water height) across the entire extent of the scene. This approach builds on the fact that emerged intertidal areas will have higher near-infrared (NIR) reflectance values, which will then abruptly drop at the moment they are submerged [71,72]. However, there are expectable differences in the tidal stages across the entire Bijagós Archipelago as it extends over ca. 100 km in latitude and longitude, which will affect the estimation of the elevations. To overcome this, we followed the method developed by Granadeiro et al., (2021) and estimated the tide lags for the whole study area. Analyses were carried out using the *mgcv* and *nplr* packages [74,75] in R and are detailed in Granadeiro et al., (2021). We thus obtained a DEM of the intertidal area corrected for tidal lags, to be used as a predictor in the supervised classifications.

The lowest tide height used to extract the intertidal area was 1.04 m (referenced to hydrographic zero; see Section 2.5.4), but the tide heights in the images selected for the classification were higher (Sentinel-1 image was acquired at a tide height of 1.11 m; Sentinel-2 at 1.55 m). To extract the final study area, we used the DEM to identify and exclude pixels that would be under water at the time of the acquisition of those images. Thus, by taking a conservative approach to reduce the chance of the inclusion of areas under water, the pixels below 1.65 m were eliminated.

2.6. Predictors for Supervised Classification

We calculated a set of indexes from Sentinel-1 and Sentinel-2 bands to act as predictors in the supervised classifications, based on their potential capacity to separate intertidal areas with different water film cover, moisture content, type of sediment, vegetation cover, and surface structure and roughness, thus discriminating the target habitat class. The list of indexes and their descriptions are presented in Table 1.

Table 1. Description of predictors considered for the supervised classifications, including a selection of relevant Sentinel-2 spectral bands, Sentinel-1 Synthetic Aperture Radar VV and VH polarisation bands, a selection of indexes derived from both sensors, and the digital elevation model produced in this study. ${\sigma_{VH}}^0$ and ${\sigma_{VV}}^0$ are the radar backscattering coefficients in decibels for the VH and VV polarisation bands, respectively, obtained during the radiometric calibration of radar intensity values.

Predictors	Sensor (Reference)	Description
Band 2—Blue (B)	Sentinel-2	Native resolution: 10 m; Central wavelength: 490 nm
Band 3—Green (G)	Sentinel-2	Native resolution: 10 m; Central wavelength: 560 nm
Band 4—Red (R)	Sentinel-2	Native resolution: 10 m; Central wavelength: 665 nm
Band 5—Vegetation Red Edge (Re1)	Sentinel-2	Native resolution: 20 m; Central wavelength: 705 nm
Band 6—Vegetation Red Edge (Re2)	Sentinel-2	Native resolution: 20 m; Central wavelength: 740 nm
Band 7—Vegetation Red Edge (Re3)	Sentinel-2	Native resolution: 20 m; Central wavelength: 783 nm
Band 8—Near Infrared (NIR)	Sentinel-2	Native resolution: 10 m; Central wavelength: 842 nm
Band 8A—Near Infrared narrow (NIRn)	Sentinel-2	Native resolution: 20 m; Central wavelength: 865 nm
Band 11—Short-wave infrared (SWIR1)	Sentinel-2	Native resolution: 20 m; Central wavelength: 1610 nm
Band 12—Short-wave infrared (SWIR2)	Sentinel-2	Native resolution: 20 m; Central wavelength: 2190 nm
NDWI—Normalised Vegetation Water Index	Sentinel-2 [73]	$(G - NIR)/(G + NIR)$
mNDWI—modified Normalised Difference Water Index	Sentinel-2 [76]	$(G - SWIR1)/(G + SWIR1)$
NDMI—Normalised Difference Moisture Index	Sentinel-2 [77]	$(NIR - SWIR1)/(NIR + SWIR1)$
nNDMI—narrow Normalised Difference Moisture Index	Sentinel-2 [78]	$(NIRn - SWIR1)/(NIRn + SWIR1)$
NDVI—Normalised Difference Vegetation Index	Sentinel-2 [79]	$(NIR - R)/(NIR + R)$
MSAVI Version 2—Modified Soil-Adjusted Vegetation Index	Sentinel-2 [80,81]	$(2NIR + 1 - \sqrt{(2NIR + 1)^2 - 8(NIR - R)})/2$
RESI—Red-edge Normalised Index	Sentinel-2 [82]	$(Re3 + Re2 - Re1)/(Re3 + Re2 + Re1)$
BSI—Bare Sediment Index	Sentinel-2 [83]	$(SWIR1 + R) - (NIR + B))/(SWIR1 + R) + (NIR + B))$
GSI—Topsoil Grain Size Index	Sentinel-2 [84]	$(R + B)/(R + B + G)$
S1-VV polarisation—vertical transmit, vertical receive	Sentinel-1	Native resolution: 5 m × 20 m, resampled to 10 m × 10 m
S1-VH cross polarisation—vertical transmit, vertical receive	Sentinel-1	Native resolution: 5 m × 20 m, resampled to 10 m × 10 m
RVI—Radar Vegetation Index	Sentinel-1	$4{\sigma_{VH}}^0/({\sigma_{VV}}^0 + {\sigma_{VH}}^0)$
S1-VH/VV—Radar Cross-polarisation ratio	Sentinel-1	${\sigma_{VH}}^0/{\sigma_{VV}}^0$
Digital Elevation Model (DEM)	Sentinel-2 [69]	Including heights ranging 1.65–4.69 m

All the satellite-derived predictors (the Sentinel-1 and Sentinel-2 bands and indexes and the DEM) were gathered in a raster stack. This enabled the extraction of the values of the pixels within the polygons from all the predictors. As a result, we obtained a dataset with a row for each pixel within each polygon, associated with their corresponding habitat types and reflectance values in each layer of the raster stack.

2.7. Supervised Classification with Random Forest Algorithm

For the supervised classifications, we used the random forest (RF) algorithm [45], an ensemble method that uses random subsets of a dataset (selected with replacement, a process called bagging) to train and grow multiple individual decision trees (classification and regression trees). During the training phase, each decision tree is grown independently, using different random subsets of the predictors and points (pixels). At each splitting node a limited, user-defined number of input predictors (*mtry*) is used. Each tree is thus trained to predict (vote) the class of new data based on the same predictors it was trained with. The majority of the votes in the forests determines the final class prediction of the RF. Random forests also take advantage of the subsets of data that were not bagged (out-of-bag samples) to validate model performance internally, using the trees to make predictions on the out-of-bag samples and obtain the out-of-bag error of the forest. This is especially useful for calculating variable importance measures and for variable selection approaches [46].

To conduct supervised classifications, we randomly split the initial predictor dataset into two subsets, one for training and the other for validation, with 70% and 30% of the data, respectively. This split was performed ensuring a similar relative abundance of each class in both new datasets. Because the polygons, which were spatially independent, contained a variable number of not spatially independent pixels, the splitting into training and validation datasets had to also take into account the polygon to which each pixel belonged, in order to preserve spatial independence the between training and validation datasets. Thus, as far as possible, all the pixels from a given polygon were included together, either in the training or the validation dataset, ensuring the independence of the final validation. This was achieved using the function *sample.split* of the package caTools in R [85].

We used the random forest function from the package with the same name in R [86] to train the RF classifiers. Two parameters of relevance can be controlled by the user: the number of trees to be grown (*ntree*, higher values produce more stable results but at the cost of computing efficiency) and the *mtry* (the number of predictors to choose at each node split). *ntree* was set to 1000 during the variable selection phase and to 5000 to run the final models. To choose the best *mtry*, we conducted tests using the initial dataset with all the predictors to run RFs cycling through a range of *mtry* values (typically from 2 to n-3, where n is the total number of predictor variables). We performed independent validations for all the models using the validation dataset and selected the *mtry* that produced the highest overall classification accuracy. The selected *mtry* was used for the subsequent runs of the RFs.

2.8. Variable Selection

Variable selection has an important influence over land cover classification exercises, particularly as a method to reduce data dimensionality and redundance and improve classification accuracy and computational efficiency and interpretability [48,87,88]. As expected, we found high (Pearson's) correlations between several of the predictors (Figure S3), supporting the need for a variable selection procedure.

Variable selection in RFs often depends on variable importance measures. Among the several measures available (see [87,89]), the permutated variable importance measure (hereafter referred to as the PVIM) is the most popular for RFs [90]. It measures the mean decrease in out-of-bag accuracy caused by permuting each variable over all the trees; the variables causing larger mean decreases are more important and can thus be ranked based on the PVIM. Performance-based variable selection algorithms implemented by R libraries, such as VSURF and varSelRF, automate this process to optimize RFs to achieve the highest accuracies [89,91,92]. However, these algorithms select the best variable set according to the predictors that together minimize the out-of-bag error. As a performance validation measure, out-of-bag error is less reliable than totally independent validations, given that each new sample is only validated by the trees that did not include them in the training phase. Moreover, out-of-bag error measures may perform inconsistently with our dataset because the spatial independence within the training dataset is greater among pixels of different polygons than among pixels of the same polygon. For these reasons, we applied a modified variable selection procedure inspired by the backward recursive feature elimination process implemented in varSelRF, but with a stricter and more demanding independent validation and variable elimination method throughout each step of the process, as described below.

The overall framework of our step-by-step variable selection process is the following: (1) start with a full model, including all the predictors, and compute an RF; (2) perform the validation of the model (using the totally independent validation dataset) and record the Overall Accuracy and Kappa Coefficient (see Section 2.12 for details on these validation statistics); (3) compute the PVIM and select the least important variable to be eliminated; and (4) repeat the process until only two predictors are left. The PVIM has, however, been shown to be potentially biased in the presence of a large number of correlated variables [48,87]. To account for this, we computed the PVIM at each step of the recursive

elimination, instead of only at the beginning. Moreover, to ensure robustness, we repeated each of the RF models with the same set of predictors 25 times and excluded the variable that featured more times as the least important at each step. The best predictor set was then chosen based on a plot of the mean Overall Accuracies and Kappa Coefficients achieved in each step, averaged over the 25 RF replicates. The Overall Accuracy and Kappa Coefficient threshold were set considering the balance of keeping the prediction accuracy high while using the minimum number of predictors, reducing redundancy, and increasing interpretability.

2.9. Variable Importance Metrics

To describe and discuss the most relevant predictors to map the intertidal habitats, we calculated the aforementioned PVIM (permutated variable importance measure), as described in Section 2.8, using the importance function of the randomForest package in R [86]. The PVIM is a measure of misclassification showing which variable causes the largest decrease in the Overall Accuracy when excluded. It is among the most robust variable importance metrics because of the permutational nature. It is calculated by subtracting, in each tree, the prediction error on the out-of-bag portion of the data by the prediction error after permuting each predictor in the out-of-bag. This is then averaged over all the trees and standardized by the standard deviation of the differences. Higher values indicate more important variables. To facilitate interpretation, the PVIM values obtained from the random forests were rescaled to values ranging between 0 and 1, these being the minimum and maximum PVIM values for each run, respectively.

2.10. Map of Intertidal Habitat Class Predictions

The map of intertidal habitats was built by applying the RF model built with the best set of predictors (hereafter referred to as the final RF model) to predict the distribution of the target habitat types for the entire study area. The area (in km^2) covered by each habitat type was also calculated.

2.11. Post-Classification Filtering

To remove the "salt-and-pepper" noise, which is common in RF supervised classifications based on medium-high resolution images, we applied a median filter (window of 3×3 pixels) to the map of the habitat class predictions (using the SAGA software v. 2.1.4; [93]). This filtering technique is simple and easy to apply, while remaining effective at removing noise and in improving the overall look of the land cover maps. Although more complex and advanced techniques have been developed for post-classification processing aiming at improving classification accuracy [94–96], their application can be very complex and thus difficult to replicate, while not being significantly better than median filters in removing noise. Taking this into consideration, we chose to apply the median filter, as the improvement of the classification accuracy of unfiltered prediction maps provided by filtering techniques has been shown to be greater than the difference in performance between these and the more complex techniques [97].

2.12. Validation and Assessment of Model Approach

Model validation was performed by comparing the independent validation dataset with the prediction results using confusion matrices and calculating the performance statistics, namely the Overall Accuracy and the Kappa Coefficient, used to access the overall performance and the quality of the models, the Producer's Accuracy (omission errors), and the User's Accuracy (commission errors), calculated for each habitat class. The Overall Accuracy is the percentage of correctly classified pixels when considering all pixels. The Kappa Coefficient describes how much better the classification produced is when compared to a classification produced purely by chance, with values ranging between 0 (no better than a random classification) and 100 (100% better). The Producer's Accuracy is the number of true positives divided by the total number of predictions within a class,

expressed as the percentage of pixels of a certain habitat class that were correctly predicted. It describes for each habitat class the probability (expressed as a percentage) of a random pixel in the field being correctly classified on the map. The User's Accuracy for each habitat class describes the probability (expressed between 0 and 100) of a random pixel on the map corresponding with the same habitat class on the ground [98–102]. See Table S2 for details on the equations of all the performance statistics used.

To assess and quantify the advantages of associating Sentinel-2 with Sentinel-1 and DEM to map the intertidal areas, we compared the final model with three other starting models: a model using only Sentinel-2 bands and indexes, a model including Sentinel-2 and Sentinel-1 imagery, and a model including Sentinel-2 and DEM information layers. The three models were subjected to the same workflow, and the comparisons with the best model were made by comparing their Overall Accuracies and Kappa Coefficients.

3. Results

3.1. Extent of Intertidal Area of the Bijagós Archipelago

From the Sentinel-2 tidal time-series images, considering water heights ranging from 1.04 m to 4.69 m, we extracted the intertidal area of the Bijagós Archipelago Biosphere Reserve, which amounted to 450.2 km^2. When considering a water height of 1.65 m (see 2.5.5 in methods), the extent of the final study area was estimated at 426.8 km^2.

3.2. Field Reference Data and Definition of Shorebird Intertidal Habitats

A total of 1023 polygons, corresponding to 25,841 pixels (10 × 10 m), were sampled within the 170 sampling sites defined throughout the intertidal flats of the Bijagós Archipelago (Figure 1). This represented 0.6% of the total intertidal area considered in this study. Overall, 580 sediment samples were analysed, representing 766 polygons and 21,649 pixels of exposed sediments. In these sediment samples, the mud content ranged between 0 and 75%, but samples with more than 30% were very scarce (Figure S4). Therefore, we created two sediment classes: sandy, with 0–10% mud content, and mixed, in which we grouped all the sediment samples with 10% or more of mud content. Using the quantitative data collected during the ground truthing and the results from the sediment analysis, we defined seven intertidal habitat types for the supervised classifications, based on a set of percent cover thresholds (rocks, shell beds, macroalgae, and FCB) and mud content (Table 2).

Table 2. Habitat types defined for the supervised classifications of intertidal habitats, with a description of the defining thresholds and features (from the field reference data and sediment analysis) and sample sizes (polygons and pixels). Mud content is the percentage weight of sediment <63 µm. FCB: fiddler crab burrow areas.

Habitat Types	Defining Thresholds	Median Water Film Cover (%)	Mud Content (Mean % ± SD)	n Polygons	n Pixels
Rocks	≥30% of rock cover.	0	N/A	88	428
Shell beds	≥30% of shell cover.	20	N/A	53	609
Macroalgae	≥30% of macroalgae cover and ≤50 FCB cover.	30	N/A	116	3155
Bare sediment sandy	≤50% of high-density FCB cover and ≤30% of rocks, shells, and macroalgae cover and <10% of mud content.	35	2 ± 2.3	408	12,777
Bare sediment mixed	≤50% of high-density FCB cover and ≤30% of rocks, shells, and macroalgae cover and ≥10% of mud content.	30	15.3 ± 6.5	36	1219
FCB sandy	≥50% of high-density FCB cover and ≤30% of rocks, shells, and macroalgae cover and <10% of mud content.	0	4.7 ± 2.9	179	4119
FCB mixed	≥50% of high-density FCB cover and ≤30% of rocks, shells, and macroalgae cover and ≥10% of mud content.	5	19.9 ± 10.3	143	3534

3.3. Variable Selection and Final Random Forest Model

The stepwise backward variable selection process resulted in high values of the Overall Accuracy and the Kappa Coefficients (starting in average at 81% and 72%, respectively, with 24 predictors) until 14 predictors remained in the model. From that point, these values started to decrease, until they reached the Overall Accuracy and the Kappa Coefficients of 62% and 43.0%, respectively, with two predictors (Figure 2). The last variables kept in the process were nNDMI and NDWI, but the removal of the DEM, Re1, and S1-VH caused the largest drops in the Overall Accuracy and the Kappa Coefficient (Table S3). To maximise the classification accuracy, we selected the RF model with 14 predictors.

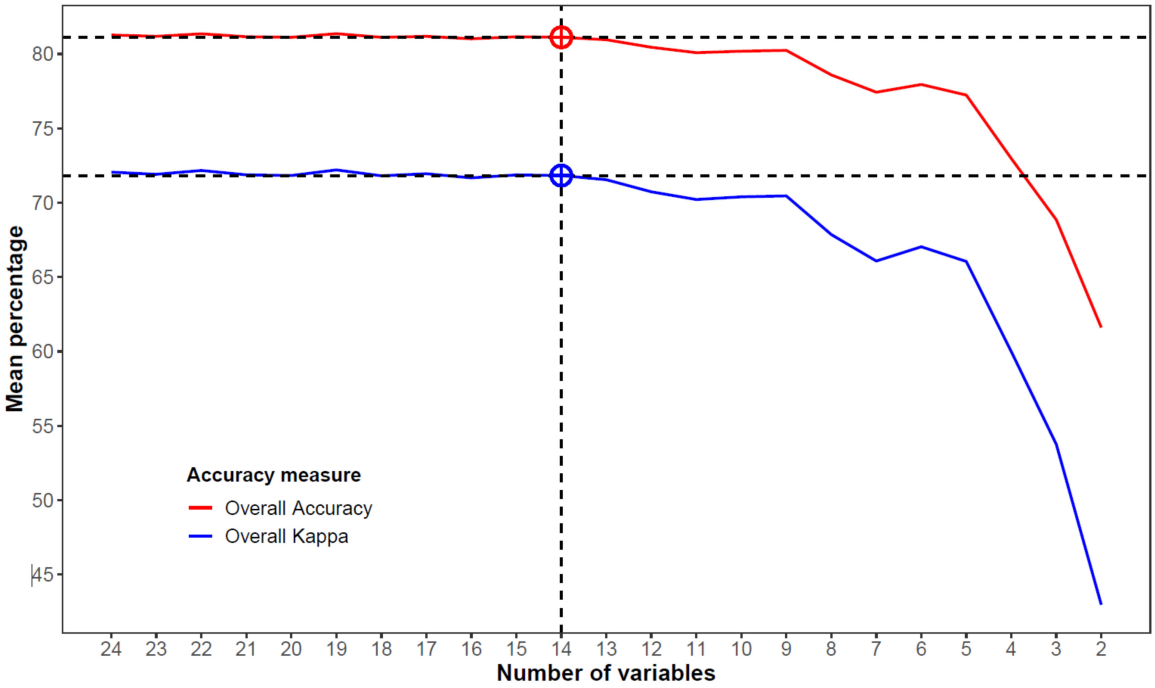

Figure 2. Variation in mean Overall Accuracy and mean Kappa Coefficient along the stepwise backward variable selection procedure. In each step, 25 random forests were computed, and an independent validation was performed for each. The red circle and dashed line mark the threshold point selected as the best variable set (14 predictors) to perform the supervised classification.

This predictor set was thus used to compute the final RF with 5000 trees, which achieved an Overall Accuracy of 81% and a Kappa Coefficient of 72% (Table 3). At the class level, the classification accuracies achieved at least 70% for most habitat types. The few exceptions were the User's Accuracy for rocks (69%), and the Producer's Accuracies for shell beds (59%) and bare sediment mixed (36%). The highest User's Accuracy was observed for shell beds (91%), while bare sediment sandy scored the highest Producer's Accuracy (93%). This model was used to generate the final classification for the entire intertidal area.

Table 3. Confusion matrix and independent validation statistics of the final random forest model, computed with the best set of predictors (14 predictors). All the values of the validation statistics range between 0 and 100%. FCB: fiddler crab burrow areas.

Predictions	Reference								
	Rocks	Shell Beds	Macroalgae	Bare Sediment Sandy	Bare Sediment Mixed	FCB Sandy	FCB Mixed	Total	User's Accuracy
Rocks	95	0	41	1	0	0	0	137	69.3
Shell beds	3	107	0	8	0	0	0	118	90.7
Macroalgae	7	3	685	23	3	3	90	814	84.2

Table 3. *Cont.*

Predictions	Reference								
	Rocks	Shell Beds	Macroalgae	Bare Sediment Sandy	Bare Sediment Mixed	FCB Sandy	FCB Mixed	Total	User's Accuracy
Bare sediment sandy	14	56	184	3573	219	192	26	4264	83.8
Bare sediment mixed	0	0	18	2	132	32	4	188	70.2
FCB sandy	1	8	11	186	4	929	168	1307	71.1
FCB mixed	8	9	8	40	8	80	772	925	83.5
Total	128	183	947	3833	366	1236	1060	7753	-
Producer's Accuracy	74.2	58.5	72.3	93.2	36.1	75.2	72.8	-	
Overall Accuracy									81.2
Kappa Coefficient									71.9

3.4. Variable Importance

The DEM was the most important variable in the final model when considering the overall PVIM values, followed by the water-related indexes nNDMI and NDWI and by the S1-VH SAR band (Figure 3). On the other hand, although still providing important contributions to the performance of the final RF classifier, the SAR indexes RVI and VH/VV, the soil index GSI, and the blue band (B) were the predictors causing the smallest decreases in mean Overall Accuracy when excluded from training data. At the classes level, the predictors displayed different levels of importance among the habitat types (Table S4). Nevertheless, the DEM was also among the two most important predictors for all habitat types except for rocks, for which the water-related predictors and the radar's S1-VH were the most relevant. Similarly, S1-VH was among the four most important across most habitat types, except for macroalgae. Finally, surface water content played an important role in separating some habitat types, with nNMDI and NDWI displaying overall high importance scores across most habitat types (Table S4).

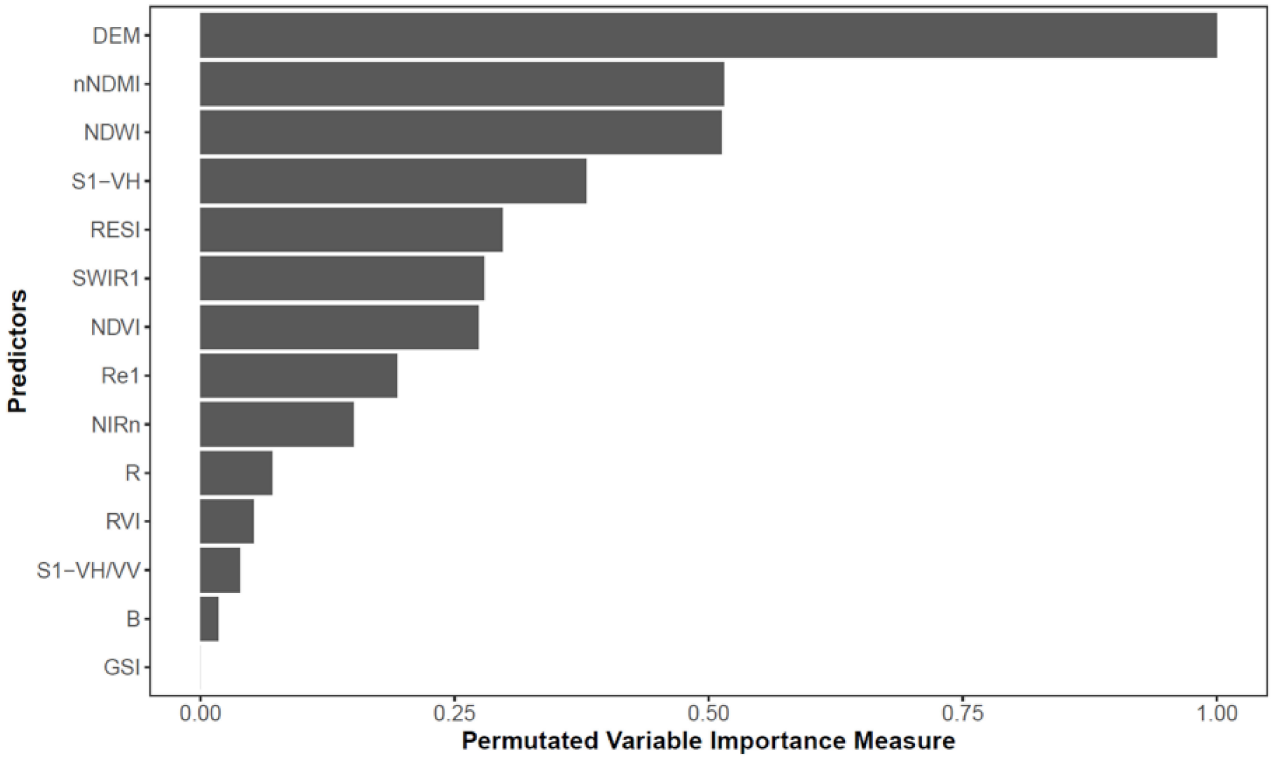

Figure 3. Permutated variable importance measure (PVIM) obtained with the final random forest model including the best predictors set (14 predictors). Values presented were rescaled in relation to the maximum value, to range between 0 and 1 (see methods). Predictor acronyms are described in Table 2.

3.5. Post-Classification Filtering

The application of the median filter resulted in marginal improvements of the Overall Accuracy and the Kappa Coefficient and of the User's and Producer's Accuracies for most habitat types (Table 4). The User's Accuracy for macroalgae and the Producer's Accuracy for rocks showed the most notable improvements (+4.1% and +2.4%, respectively), while decreases were observed only in two instances, namely for the User's Accuracies of the rocks (−3.1%) and shell beds (−0.6%; Table 4).

Table 4. Comparison of independent validation statistics between unfiltered and filtered intertidal habitat distribution maps, produced from the prediction made with the final random forest model with the 14 best predictors. Numbers in bold signal the highest score.

Stats		Unfiltered	Filtered
Overall Accuracy		81.2	**81.8**
Kappa Coefficient		71.9	**73.1**
Rocks	User's Accuracy	**69.3**	66.2
	Producer's Accuracy	74.2	**76.6**
Shell beds	User's Accuracy	**90.7**	90.1
	Producer's Accuracy	58.5	**59.6**
Macroalgae	User's Accuracy	84.2	**88.3**
	Producer's Accuracy	72.3	**73.8**
Bare sediment sandy	User's Accuracy	83.8	83.8
	Producer's Accuracy	93.2	**93.6**
Bare sediment mixed	User's Accuracy	70.2	**72.4**
	Producer's Accuracy	36.1	**36.7**
Fiddler crab burrow sandy	User's Accuracy	71.1	**72.3**
	Producer's Accuracy	75.2	**75.4**
Fiddler crab burrow mixed	User's Accuracy	83.5	**84.0**
	Producer's Accuracy	72.8	**75.1**

3.6. Analysis of the Final Intertidal Habitat Prediction Map

The final prediction map with the distribution of the intertidal habitats in the study area is presented in Figure 4 (see also Figure S5). Figures 5 and 6 show detailed views of the example areas with details for each habitat type. The intertidal flats of the Bijagós Archipelago comprise mostly exposed sediments (83.1%), followed by 11.6% of macroalgae cover (Table 5). Bare sediment sandy habitats had the largest extension (59.1% of the study area), whereas bare sediment mixed habitats were the rarest (1.9%). Areas covered by fiddler crab burrows (sandy or mixed) totalled 22.1% of the study area (and 26.6% of the surface area represented by exposed sediments). Bare sediment areas, macroalgae, and shell beds showed to be related to wetter areas (median water film covers of 30–35%, 30%, and 20%, respectively, within the reference dataset), whereas the FCB sediments and rocks were associated with the dryer areas (median water film cover of 0–5% and 0%, respectively, Table 2). This is further supported by the reflectance of water-related indexes for these habitat types in our training dataset, with higher mean values (indicating higher water or moisture content) observed for the bare sediment areas, macroalgae, and shell beds and lower values for the FCB areas and rocks (Figures 7 and S6). Because the macroalgae areas have high water-film cover, several pixels bordering the intertidal flats seemed to be misclassified as macroalgae. Nevertheless, macroalgae often appear alongside the FCB areas. On average, the FCB areas had overall higher elevations (based on the DEM) than the bare sediment areas (2.42 m vs. 2.33 m). Within both the bare sediment and the FCB areas, there were contradictory patterns when comparing the mean elevations between the sandy and mixed sediments, with the mixed sediments presenting higher elevations in the bare sediment areas, while the sandy sediments were more elevated in the FCB areas (Figure 7).

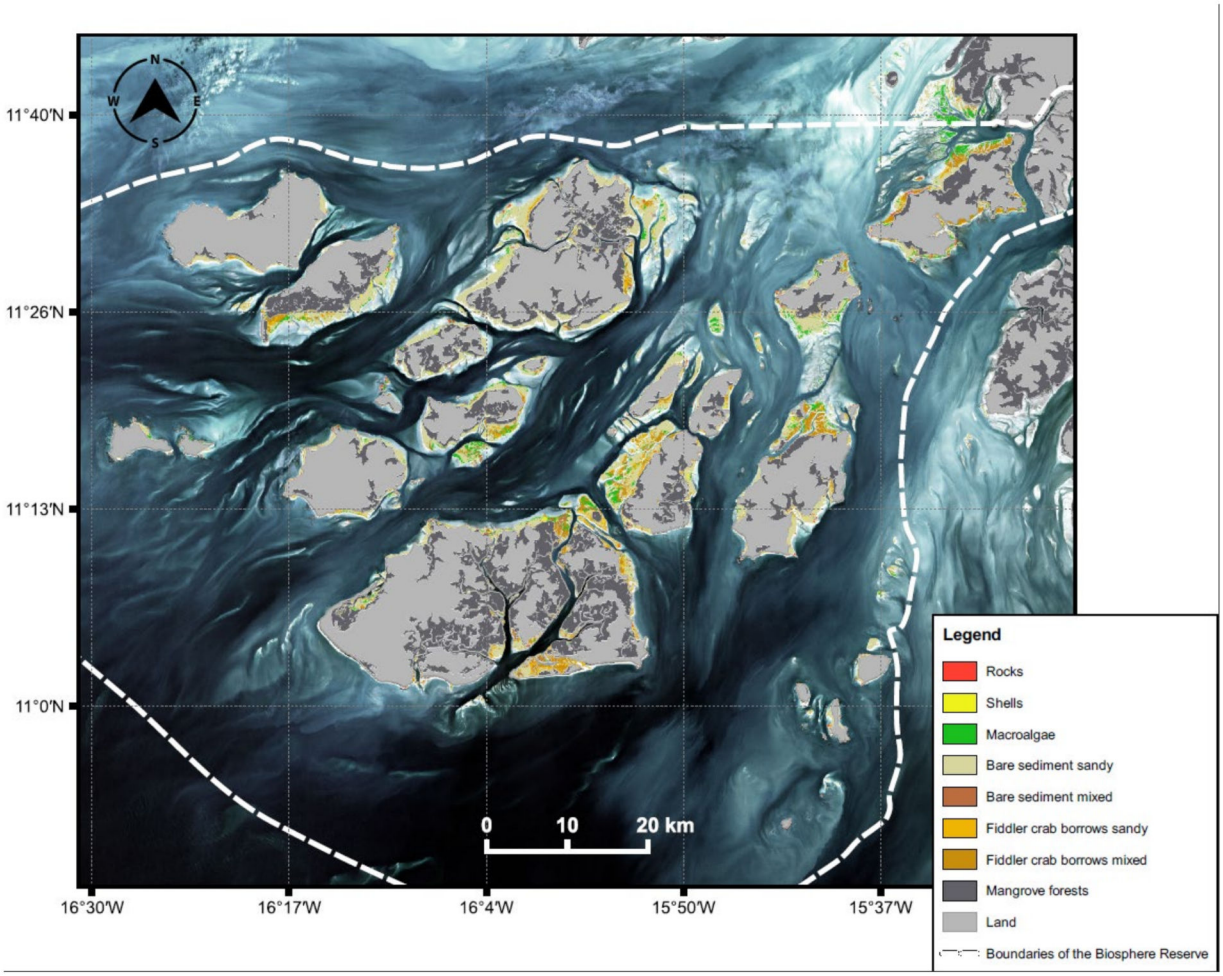

Figure 4. Map of the distribution of seven intertidal habitat types of the Bijagós Archipelago, generated with the final random forest model (14 predictors).

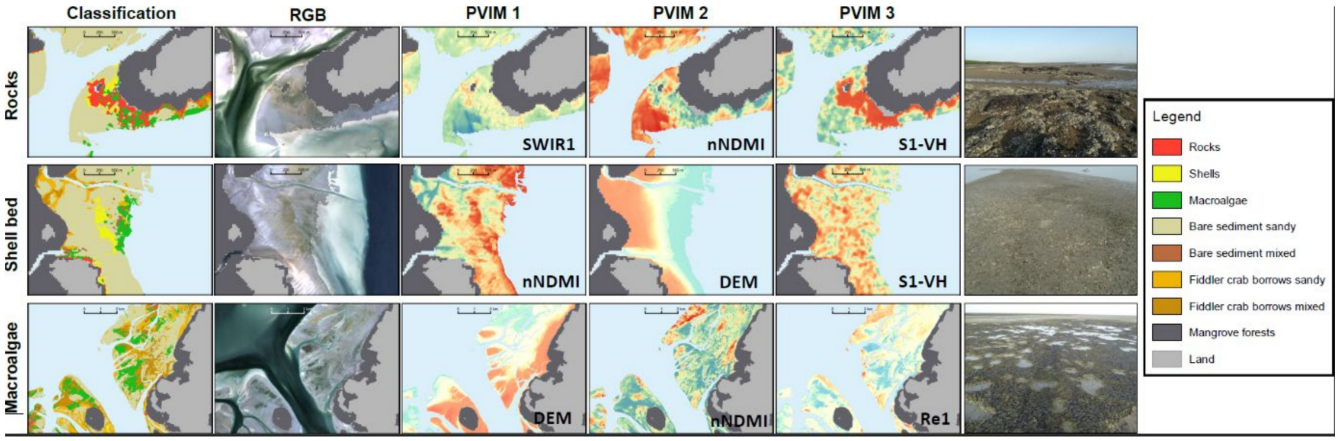

Figure 5. Detailed view of example areas for rocks, shell beds, and macroalgae habitats, with visual comparison to an equivalent RGB image produced from the same Sentinel-2 image for which predictions were conducted to produce the final map. The three most important predictors for each habitat type are shown in order of importance according to the permutated variable importance measure (PVIM 1, PVIM 2, and PVIM 3), with a spectral colour pallet ranging from blues for smaller values, yellows for intermediate values, and orange-red for higher values. Last column presents example images from the ground.

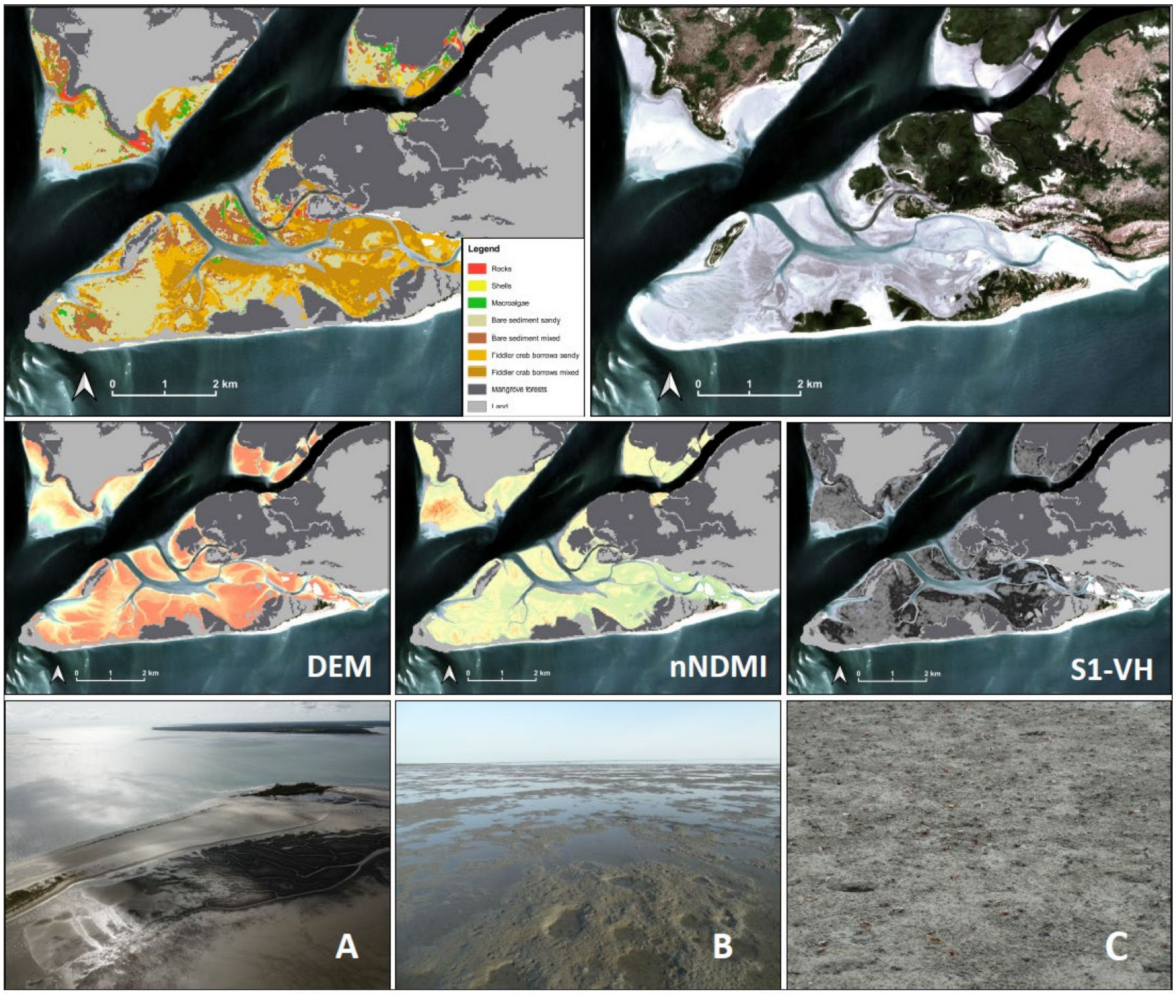

Figure 6. Detailed view on an example area for sandy and mixed sediments within bare sediment and fiddler crab burrow (FCB) areas, with visual comparison to an equivalent RGB image (with linear colour stretch) produced from the same Sentinel-2 image for which predictions were conducted to produce the final map. Maps of the three most important predictors to classify these habitat types are shown for the same area (DEM, nNDMI, and S1-VH). Colours for DEM and nNDMI range from blue for lowest, yellow for intermediate, and orange-red for highest values. S1-VH are represented in grey-scale values. Dark blue areas represent the water mask, light grey areas represent the land mask (excluding mangroves), and dark grey areas represent mangroves. (**A**) Aerial photograph of the example area, showing the striking visual difference between bare sediment and FCB habitats; (**B**,**C**) show photographs of on the ground examples of bare sediment and FCB habitats, respectively.

Table 5. Estimates of the total area (in km^2 and in % of the total) covered by each intertidal habitat, produced from the final map predictions with the final model (14 predictors). FCB: fiddler crab burrow areas.

Habitat Type	Area (km^2)	% of Total
Rocks	15.7	3.7
Shell beds	6.7	1.6
Macroalgae	49.6	11.6
Bare sediment sandy	252.3	59.1
Bare sediment mixed	7.9	1.9
FCB sandy	38.2	8.9
FCB mixed	56.3	13.2
Total	426.8	100.0

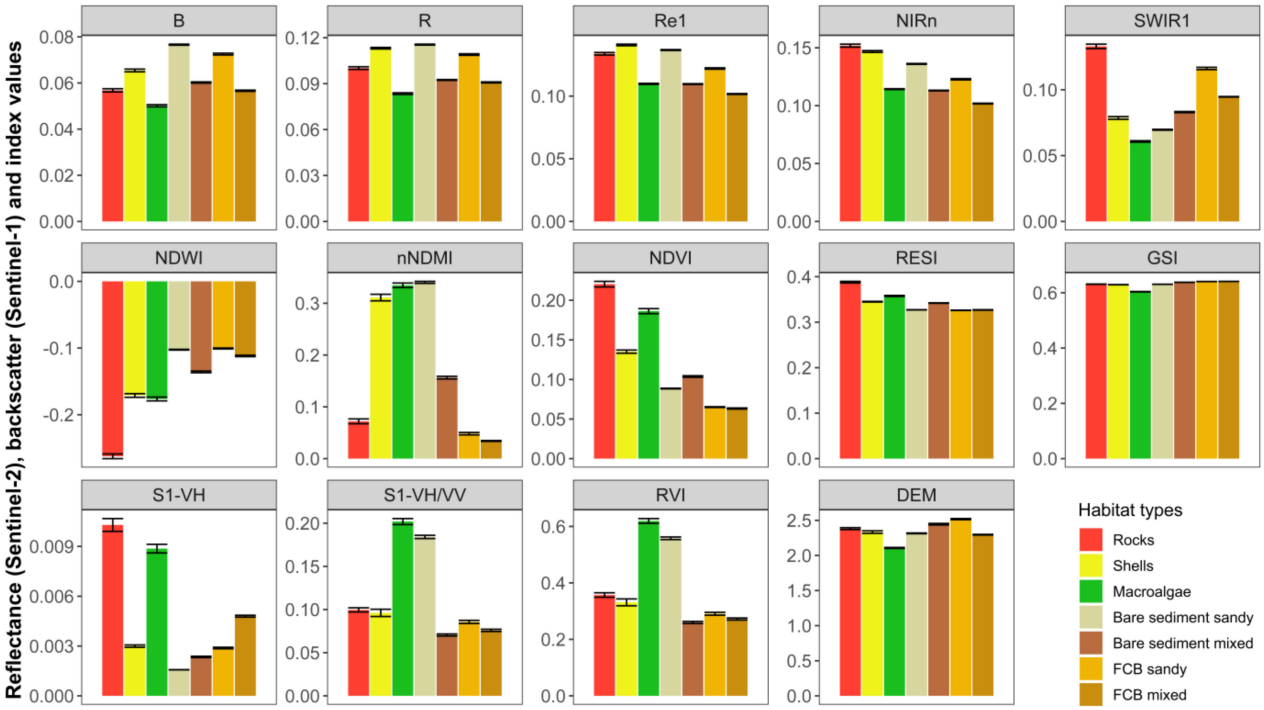

Figure 7. Mean ± SE reflectance, backscatter, and index values of the 14 best predictors for each of the seven habitat types classified in the intertidal flats of the Bijagós Archipelago.

3.7. Comparison between Final Model and Models without Sentinel-1 and DEM

Our final RF model with Sentinel-1, Sentinel-2, and the DEM produced classifications with the highest Overall Accuracy and Kappa Coefficient, when compared to models without Sentinel-1 and the DEM (Table 6). Likewise, it generally outperformed the other models on most occasions at the habitat class level (Table 6). The alternative model that achieved the closest performance to our final model was the one associating Sentinel-1 and Sentinel-2 predictors, while the poorest performance was delivered by the model including only Sentinel-2 predictors (Table 6).

Table 6. Comparison of model performance between the model associating Sentinel-1, Sentinel-2, and DEM and three alternative models: using Sentinel-2 alone (S2 model); model using Sentinel-2 and Sentinel-1 (S2 + S1 model); and a model including Sentinel-2 and the digital elevation model. All alternative models were computed using the same workflow applied to obtain the best model. Performance statistics were calculated from independent validation with the training dataset and are based on unfiltered outputs. FCB: fiddler crab burrow areas. Numbers in bold signal the highest score.

Stats		Final Model S2 + S1 + DEM 14 Predictors	S2 Model 14 Predictors	S2 + S1 Model 14 Predictors	S2 + DEM Model 16 Predictors
Overall Accuracy		**81.2**	77.3	80.3	78.4
Kappa		**71.9**	66.1	70.6	67.5
Rocks	User's Accuracy	69.3	**92.9**	75.2	88.2
	Producer's Accuracy	**74.2**	61.7	68.8	64.1
Shell beds	User's Accuracy	90.7	59.9	**91.7**	72.4
	Producer's Accuracy	**58.5**	48.1	54.7	53.0
Macroalgae	User's Accuracy	**84.2**	75.7	82.7	79.3
	Producer's Accuracy	72.3	77.5	72.0	**78.7**

Table 6. *Cont.*

Stats		Final Model S2 + S1 + DEM 14 Predictors	S2 Model 14 Predictors	S2 + S1 Model 14 Predictors	S2 + DEM Model 16 Predictors
Bare sediment sandy	User's Accuracy	**83.8**	80.9	83.4	81.3
	Producer's Accuracy	**93.2**	90.9	93.0	92.1
Bare sediment mixed	User's Accuracy	**70.2**	58.0	60.3	62.2
	Producer's Accuracy	**36.1**	28.7	32.8	27.9
FCB sandy	User's Accuracy	**71.1**	67.1	70.5	67.3
	Producer's Accuracy	**75.2**	63.3	71.6	64.9
FCB mixed	User's Accuracy	**83.5**	80.4	80.8	81.0
	Producer's Accuracy	72.8	68.1	**74.1**	67.6

4. Discussion

In this study, we mapped for the first time a set of intertidal habitats of relevance to shorebirds in one of the most important non-breeding areas of the East Atlantic Flyway of the Bijagós Archipelago. We applied a workflow that combines multispectral and SAR sensors, using well-established, semi-automated machine learning methods. This resulted in the successful classification of seven intertidal habitat types, namely rocks, shell beds, macroalgae, and two types of sediment (sandy and mixed, based on mud content) within bare sediment areas and areas with fiddler crab burrows (FCB). This large-scale mapping provides an important product for future monitoring of this high biodiversity area, particularly for ecological research related to the distribution, movement, and feeding ecology of shorebirds and their prey.

4.1. Classification Performance

Using a stringent validation procedure (based only on polygons that were not used for classification), we achieved an Overall Accuracy of ca. 82% and a Kappa Coefficient of ca. 73% when classifying seven distinct intertidal habitat types. These indicators suggest a high quality classification, comparable to other similar studies for intertidal habitat mapping (e.g., [29,43,103–106]).

Remotely sensed mapping of intertidal areas is particularly challenging, especially when distinguishing different sediment types and can be hindered by the spectral similarities between sediment types with different grain sizes and by the presence of water. For example, by combining RapidEye (a multispectral instrument with 5 m spatial resolution) and TerraSAR-X (a SAR instrument with 1 m spatial resolution) Jung et al., (2015) justified achieving lower classification accuracies for intertidal sediment areas than for intertidal vegetation and shellfish beds with the presence of water on the sediment. Likewise, Kim et al., (2019) achieved accuracies limited to ca. 73% when attempting to classify six types of sediments using a very high spatial resolution (0.26 m) RGB orthoimage (from a CMOS sensor of a DSLR camara mounted on an unmanned aerial vehicle), due to the spectral similarities between the different sediment classes. Ref. [107] attained only 65% when using Sentinel-1 and Sentinel-2 to map three classes of sediment clay content.

In our study, we successfully mapped two sediment types (sandy and mixed) for both the bare sediment and the FCB areas, with User's and Producer's Accuracies above 72% for all sediment types, except for bare sediment mixed, for which we only achieved 37%. Most of the pixels of this habitat type in the validation dataset were incorrectly classified as bare sediment sandy. Both bare sediment habitats (sandy and mixed) had the highest water film cover and high reflectance for the water and moisture-related indexes, which can explain the confusion between these two. Moreover, bare sediment mixed was among the rarest habitat types, both in our field reference data and in the final prediction map (1.9% of the total area); hence, it had considerably fewer data for training the RF algorithm. These two

factors might explain the poor performance when classifying the bare sediment mixed class but a good performance when predicting bare sediment sandy areas.

Despite the overall positive results in mapping sediment in terms of mud content, the separation of sediment types into only two classes based on mud content may be too simplistic from the perspective of the benthic invertebrates and the shorebirds that feed on them. Previous studies successfully classified a higher number of intertidal sediment classes, but these often involved the use of higher resolution imagery [31,103,108], or their workflows were fully optimized to be focused only on sediment mapping, using SAR [32,109] or DSLR cameras mounted on unmanned aerial vehicles [103]. The use of higher resolution satellite data may help to increase the number of sediment classes, but these products often have much less radiometric resolution or are of limited access or may come at very high monetary and computational costs (see [29]). In addition, the exclusive focus on sediment types will likely disregard other important intertidal habitats. We believe our approach constitutes a good balance between performance and replicability in our study area.

4.2. Multi-Sensor Approach and Variable Importance

We showed that the combination of Sentinel-1 and Sentinel-2 imagery with a detailed DEM achieves higher classification accuracies than without the association of the SAR and DEM. The SAR is useful in helping to retrieve geophysical traits in intertidal areas, and in particular, the C-band is more effective for sensing the roughness of finer sediments [110]. In our study, S1-VH, a C-band information layer, was among the most relevant in classifying different types of exposed sediments, namely in separating bare sediment and areas with high densities of fiddler crabs and, within these, distinguishing between finer (mixed) and coarser (sandy) sediments. Multispectral imagery, on the other hand, is especially useful in assessing moisture and water content [107,111] and in mapping intertidal vegetation features [27]. In our study, high water film cover was a characteristic trait in several habitat types, particularly for bare sediment areas and macroalgae, whereas the FCB areas and rocks had little to no water content. Consequently, Sentinel-2-derived moisture indexes, particularly nNDMI and NDWI, were very important in the classification of these habitat types, effectively complementing the SAR information layers.

The variable selection procedure allowed for a much clearer interpretation of the predictors and of the specific characteristics distinguishing each habitat type. The most important predictor of intertidal habitats in our study area was the DEM. Elevation models are used in land cover classification exercises to indicate topographic features, and in intertidal landscapes; they have been shown to be spatially related to sediment grain size distributions [112,113]. Choi et al., (2011) showed that fine-grained sediments tended to occur in elevated areas, while coarser sandy sediments would occur in lower areas. They also reported a strong correlation between satellite reflectance (from Landsat ETM+ imagery) and the DEM, supporting the argument that, in intertidal flats, more elevated areas (with higher exposure times) have less water content and finer grain sizes. In our study, we only found similar results in this regard within bare sediment areas, where mixed sediments (with finer grain sizes) were on average more elevated than sandy sediments and also displayed less water content, according to their reflectance in water and moisture content indexes. However, in the FCB areas the pattern was the opposite, with sandy sediment displaying higher mean elevations and with similar water and moisture contents in the sandy and mixed sediments. Similarly, we found a significant relationship between elevation and sediment mud content in both the bare sediment and the FCB areas, but again with opposite patterns, whereas in the bare sediment areas this relationship was positive but weak (simple linear regression, $p > 0.001$, $R^2 = 0.002$) and in the FCB habitats, it was negative and stronger ($p < 0.001$, $R^2 = 0.21$). Further experimental studies analysing the role of fiddler crabs in changing intertidal sediment characteristics and topography in this area would help in clarifying these results. While the combination of Sentinel-1 and Sentinel-2 (excluding the DEM) also produced similarly high Overall Accuracy, the inclusion of the

DEM was important in vastly improving the classification of the bare sediment mixed habitats (+9.9% User's Accuracy and +3.3% Producer's Accuracy) and performed better overall for most of the remaining habitat types. This supports our recommendation to also integrate a detailed DEM, together with multispectral and SAR predictors, in intertidal habitat classification exercises.

4.3. Extent and Distribution of Intertidal Habitats

We estimated that the intertidal area of the Bijagós Archipelago extends for ca. 450.2 km^2 (for a tidal height of 1.04 m), comprising 37.4% of the total intertidal area of the country [1]. This contrasts markedly with the estimate reported for 1995 [50,51] of ca. 1200 km^2, which has been frequently cited in many studies on the Bijagós Archipelago. Our result does not include images captured at low tide during spring tides (i.e., ±2 days around new and full moons), due to the lack of acquisitions in those periods. Spring tides during the dry season (November to April) in the Bijagós Archipelago averaged 0.74 ± 0.23 m in height for the period of 2019–2021 and ranged between 0.3–1.3 m, with heights over 1 m representing ca. 26% of all spring tides in this period [114]. While our estimate represents tides slightly higher than these averages for the dry season, it still is within the range of 26% of low tides during spring tide and represents well the average heights for most low tides in the Bijagós Archipelago. Given the fact that the total intertidal area of the entire country has been estimated at ca. 1203 km^2 for 2014–2016 [1] and that the intertidal area of the Bijagós Archipelago has been reported to have increased by 115 km^2 between 1999 and 2016 [115], it is likely that 1200 km^2 is a major overestimation for this site. Our estimate was based on reproducible methods, and we suggest that it is used as the updated reference for this area.

Most of the intertidal area of our study area is composed of exposed sediments (355 km^2, ca. 83% of the study area), within which bare sediment areas were the most widespread (totalling 260 km^2). Nevertheless, almost 27% of the area of exposed sediments was occupied by fiddler crab burrows, covering 95 km^2. The extension of the total intertidal area occupied by sandy sediments far surpassed that of the mixed sediments (68% vs. 15.1%), and while this was also the case within the bare sediment areas (sandy: 59.1%; mixed: 1.9%), the opposite was observed in the FCB areas (sandy: 8.9%; mixed: 13.2%).

4.4. Implications for Shorebirds and Benthic Invertebrates

This intertidal cartography was made with a focus on identifying and quantifying habitat units of importance to shorebirds and their prey. As such, all seven habitat types are characterized by biotic and abiotic traits differentially important to shorebird species. Rock habitats are scarce in the Bijagós Archipelago and mainly border the coasts of the islands. They are nonetheless important intertidal habitats to some shorebird species such as the Common Sandpiper *Actitis hypoleucos* and Ruddy Turnstone *Arenaria interpres* [57]. Hard structures in the sediment, such as dead shell beds, may increase the substrate resistance, consequently decreasing the available space for some benthic invertebrates [56] and rendering the sediment inaccessible to probing shorebirds. However, in temperate intertidal areas, Ruddy Turnstones were reported to occur only in areas with >30% of dead shell cover [54] and Whimbrels *Numenius phaeopus* were also observed using dead oyster banks (author's pers. obs.). Macroalgae, which cover ca. 12% of the intertidal surface of the Bijagós Archipelago, may differentially affect the foraging behaviour and success of different shorebird species. Some visual foragers such as Grey Plovers *Pluvialis squatarola* have been reported to have had their foraging area reduced by macroalgae mats [58], while tactile forager species can actually benefit from macroalgae habitats, as they promote prey variability across the intertidal landscape and may additionally reduce competition from larger shorebird species [58].

Fiddler crabs occupy a quarter of the intertidal area and have been reported to be a main player in habitat partitioning in the Bijagós Archipelago for benthic invertebrate and shorebird communities [25]. This crab acts both as a key prey for certain shorebird species, such as Whimbrels *Numenius phaeopus*, Grey Plovers, and Redshanks *Tringa totanus* [7,116],

and as a regulator, likely limiting the occurrence and biomass of most harvestable macroinvertebrates, namely bivalves, polychaetes, gastropods, and other crustaceans [25]. Hence, shorebird communities are clearly segregated between areas with and without fiddler crabs, and in our map, bare sediment areas will support markedly different (and also more abundant and richer) shorebird and benthic invertebrate communities compared to the FCB areas. In fact, the ability to map the FCB habitats at the scale of the entire Bijagós Archipelago with good accuracy is one of the important contributions of this work, and to the best of our knowledge, this is the first time the distribution of fiddler crabs has been mapped with remote sensing. This opens a promising scope regarding the assessment of the spatial extent of its influence on the intertidal ecosystem through time.

Sediments with higher mud content will be potentially more attractive to certain shorebird species, as has been shown in different areas for Red Knots *Calidris canutus* [62], Grey Plovers [54], and Curlew Sandpipers *Calidris ferruginea* [116], while others will prefer sandy sediments, with less mud content, such as Sanderlings *Calidris alba* and Kentish Plovers *Charadrius alexandrinus* [54,116]. This confirms that knowledge on the distribution of these intertidal habitats and ecosystem engineers is of great importance in understanding and predicting the distribution, foraging ecology, and community composition of the shorebird assemblages in the Bijagós Archipelago.

4.5. Applications to Monitoring and Management in the Bijagós Archipelago

The cartography of the intertidal habitats produced in this study can be useful for informing several ongoing research and monitoring efforts in the Bijagós Archipelago. For example, the International Waterbird Census [10,117] has been the source of population estimates and trend assessment for migratory shorebird populations in the EAF (see [11]). In the Bijagós Archipelago, these population estimates are produced by partial counts which are then extrapolated for the entire intertidal area [16]. It is therefore essential to generate supporting knowledge to produce the best possible estimates, as adequate conservation and management decisions rely on them. A detailed map of the distribution of intertidal habitats, which is differentially important to several shorebird species, has the potential to support sampling and extrapolation stratification and thus to deliver more accurate extrapolations by considering the variations in shorebird habitat use.

This workflow shows the potential to be the basis of a habitat monitoring scheme on wide spatial scales in other key intertidal areas. It can also be applied to satellite images of different dates to assess temporal variations in the extent and distribution of key elements of intertidal habitats, such as the fiddler crab areas or the macroalgae mats. This qualifies as an important tool for aiding the assessment of future changes in the extent and configuration of shorebird habitats at a site level, especially under a scenario of rapid global change. It can also prove to be important for looking at past changes and in helping to understand current shorebird population trends.

5. Conclusions

Mapping intertidal areas using satellite imagery is a challenging task, particularly due to the spectral homogeneity of different types of substrate and to the interference of surface water with reflectance of different wavelengths. Nonetheless, tidal areas represent very important environments for a suite of bird species, including migratory shorebirds, many of which are in decline worldwide. By presenting a detailed workflow that allows the successful mapping of a considerable number of habitat classes that are potentially important for migratory shorebirds and their benthic invertebrate prey, this study contributes to the field of ecological applications of remote sensing within intertidal ecosystems. Among the relevant contributions in this study is the production of the first distribution map of fiddler crabs, an ecosystem engineer known to play an important role in shaping benthic food webs in intertidal landscapes.

Using an extensive testing and validation procedure, we showed that the application of both active and passive sensors from freely available sources (ESA's Sentinel program) and

a DEM can improve the classification accuracy in intertidal environments. This may serve as a basis for similar applications elsewhere, and we argue that the proposed workflow may be replicated in other intertidal areas, with the required methodological adjustments to the particular conditions in each area. Nevertheless, we faced challenges when trying to identify more than two sediment types, and further improvements, e.g., considering more complex, textural, and spatial-dependent sediment descriptors (e.g., [103]) and other thresholding techniques, should now be explored.

Supplementary Materials: The following supporting information can be downloaded at: https://www.mdpi.com/article/10.3390/rs14143260/s1, Table S1. Sentinel-2 satellite image time-series selected to produce the water and land mask, and the digital elevation model. For each date (n = 29), two adjacent scenes were downloaded (T28PCT and T28PDT), totalling 58 images. Tidal heights (water height at the exact time of image acquisition) for each image were calculated following the methods described in [69]. Table S2: Performance statistics and respective equations. TP: true positives (fraction of pixels that are correctly classified as belonging to their true class). TN: true negatives (fraction of pixels correctly classified as not belonging to a class. FP: false positives (fraction of pixels wrongly classified in a class). FN: false negatives (fraction of pixels wrongly classified as not belonging to a class). Ao: observed Accuracy (true proportion of correctly classified pixels in relation to all pixels). Ae: expected Accuracy (the accuracy that would be expected to be achieved by the classifier purely by chance). i: any given class. Table S3. Results of the stepwise backward variable selection, with mean, min and max validation statistics (n = 25 random forests for each predictors set). Each row represents one step of the backward selection. Overall Accuracy and Kappa Coefficient values range between 0 and 100%. Least important variable shows the predictors with the highest % of votes as the least important throughout the 25 random forests, in each step (and therefore, the next variable to remove). The last variable kept was nNDMI. N/A: not applicable. Table S4. By-class permutated variable importance measure (PVIM) for each predictor used in the final model (with 14 predictors). Values presented were rescaled in relation to the maximum value, to range between 0 and 1. Predictor acronyms are described in Table 2 of the main article. BS: Bare sediment areas. FCB: Fiddler crab burrow areas. Figure S1. Visual representation of two merged Sentinel-2 scenes before (A) and after (B) scene intercalibration. Scene intercalibration was performed by computing a major axis regression on the area of the image where the two scenes coincide and rescaling one of the scenes to the range of values of the reference scene (see methods). Figure S2. Map with the temporal variability (standard deviation) of the Normalized Difference Water Index (NDWI) used to extract the intertidal region in our study area. The threshold used to identify the intertidal region was 0.2. Figure S3. Pearson's correlation matrix between all considered predictors. "X" signals non-significant correlations (for a 95% confidence interval). Figure S4. Histogram of mud content (% of sediment with grain size < 63 μm), coloured by sediment types according to [2], adapted from Folk et al., (1970). Figure S5. Map of the digital elevation model of the intertidal areas of the Bijagós Archipelago, with measures of the intertidal extent of natural geographic units within the study area. Figure S6. Mean reflectance values of the 14 best predictors used to classify seven intertidal habitat types of relevance to migratory shorebirds in the Bijagós Archipelago, Guinea-Bissau.

Author Contributions: Conceptualization, M.H., J.P.G., T.C., J.R.B. and T.P.; data curation, M.H. and J.R.B.; formal analysis, M.H., J.R.B. and J.P.G.; funding acquisition, T.C., J.P.G., T.P. and S.P.; investigation, M.H., J.R.B., J.P.G., T.C. and T.P.; methodology, M.H., J.R.B., J.P.G. and T.C.; project administration, T.C., S.P. and J.P.G.; resources, T.C., J.P.G., S.P. and T.P.; supervision, J.P.G., T.C. and T.P.; visualization, M.H., J.R.B., J.P.G., T.C. and T.P.; writing—original draft, M.H.; writing—review and editing, T.C., J.R.B., T.P., J.P.G. and S.P. All authors have read and agreed to the published version of the manuscript.

Funding: This work was supported by the MAVA Foundation through the project "Waders of the Bijagós: Securing the ecological integrity of the Bijagós Archipelago as a key site for waders along the East Atlantic Flyway". Fundação para a Ciência e Tecnologia (FCT Portugal) provided additional financial support to CESAM (UIDP/50017/2020 + UIDB/50017/2020 + LA/P/0094/2020) and through the project "MigraWebs: Migrants as a seasonal ecological force shaping communities and ecosystem functions in temperate and tropical coastal wetlands" (PTDC/BIA/ECO/28205/2017). M.H. and T.C. were supported by FCT through doctoral grants (SFRH/BD/131148/2017 and COVID/BD/151924/2021) and contract (2021.00573.CEECIND), respectively.

Data Availability Statement: Data supporting the reported results can be made available upon reasonable request by contacting the authors directly.

Acknowledgments: Thanks are due to the Instituto da Biodiversidade e das Áreas Protegidas Dr. Alfredo Simão da Silva (Guinea-Bissau), namely to Justino Biai, Aissa Regalla, Quintino Tchatchalam, Emanuel Dias and Saído Gomes, and to Tiniguena-Esta Terra é Nossa, namely Emanuel Ramos, Nela, Sebastião, Toni, Nfali, and Abdu for providing the permissions and logistical support needed during field work. We also thank all collaborators that helped us during this work, namely Seco Leão, Caramó, Filipe Moniz, and João Paulino for critical help in the field. We thank MARE/FCUL, namely Paulo Sousa and João Paulo Medeiros, for advice and for granting access to the sediment analysis laboratory. We are grateful to Augusta Henriques, Pierre Campredon, Mimi and Nélson for providing support during our stay on the field. Finally, we thank João Catalão, Paulo Cardoso, Francisco Andrade, and Ruth Howison for valuable advice on remote sensing subjects.

Conflicts of Interest: The authors report there are no conflict of interest to declare.

References

1. Murray, N.J.; Phinn, S.R.; DeWitt, M.; Ferrari, R.; Johnston, R.; Lyons, M.B.; Clinton, N.; Thau, D.; Fuller, R.A. The global distribution and trajectory of tidal flats. *Nature* **2019**, *565*, 222–225. [CrossRef] [PubMed]
2. Beninger, P.G. *Mudflat Ecology*; Beninger, P.G., Ed.; Aquatic, Ec.; Springer International Publishing: Cham, Switzerland, 2018; ISBN 978-3-319-99192-4.
3. van der Zee, E.M.; Angelini, C.; Govers, L.L.; Christianen, M.J.A.; Altieri, A.H.; van der Reijden, K.J.; Silliman, B.R.; van de Koppel, J.; van der Geest, M.; van Gils, J.A.; et al. How habitat-modifying organisms structure the food web of two coastal ecosystems. *Proc. R. Soc. B Biol. Sci.* **2016**, *283*, 20152326. [CrossRef] [PubMed]
4. van Gils, J.A.; van der Geest, M.; Jansen, E.J.; Govers, L.L.; de Fouw, J.; Piersma, T. Trophic cascade induced by molluscivore predator alters pore-water biogeochemistry via competitive release of prey. *Ecology* **2012**, *93*, 1143–1152. [CrossRef] [PubMed]
5. Booty, J.M.; Underwood, G.J.C.; Parris, A.; Davies, R.G.; Tolhurst, T.J. Shorebirds Affect Ecosystem Functioning on an Intertidal Mudflat. *Front. Mar. Sci.* **2020**, *7*, 685. [CrossRef]
6. van de Kam, J.; Ens, B.; Piersma, T.; Zwarts, L. *Shorebirds: An Illustrated Behavioural Ecology*; KNNV Publishers: Utrecht, The Netherlands, 2004.
7. Lourenço, P.M.; Catry, T.; Granadeiro, J.P. Diet and feeding ecology of the wintering shorebird assemblage in the Bijagós archipelago, Guinea-Bissau. *J. Sea Res.* **2017**, *128*, 52–60. [CrossRef]
8. Stroud, D.A.; Baker, A.; Blanco, D.E.; Davidson, N.C.; Delany, S.; Ganter, B.; Gill, R.; González, P.; Haanstra, L.; Morrison, R.I.G.; et al. *The conservation and population status of the world's waders at the turn of the millennium In Waterbirds around the World*; Boere, G.C., Galbraith, C.A., Stroud, D.A., Eds.; The Stationery Office: London, UK, 2006; pp. 643–648.
9. Sutherland, W.J.; Alves, J.A.; Amano, T.; Chang, C.H.; Davidson, N.C.; Max Finlayson, C.; Gill, J.A.; Gill, R.E., Jr.; González, P.M.; Gunnarsson, T.G.; et al. A horizon scanning assessment of current and potential future threats to migratory shorebirds. *Ibis* **2012**, *154*, 663–679. [CrossRef]
10. *East Atlantic Flyway Assessment 2017: The Status of Coastal Waterbird Populations and Their Sites*; Van Roomen, M.; Nagy, S.; Citegetse, G.; Schekkerman, H. (Eds.) Wadden Sea Flyway Initiative; Wetlands International; Wadden Sea Flyway Initiative: Wilhelmshaven, Germany; Wetlands International: Wageningen, The Netherlands; BirdLife International: Cambridge, UK, 2018.
11. Oudman, T.; Schekkerman, H.; Kidee, A.; Van Roomen, M.; Camara, M.; Smit, C.; Horn, J.T.; Piersma, T.; El-Hacen, E.H.M. Changes in the waterbird community of the Parc National du Banc d'Arguin, Mauritania, 1980–2017. *Bird Conserv. Int.* **2020**, *30*, 618–633. [CrossRef]
12. van Gils, J.A.; Lisovski, S.; Lok, T.; Meissner, W.; Ozarowska, A.; de Fouw, J.; Rakhimberdiev, E.; Soloviev, M.Y.; Piersma, T.; Klaassen, M. Body shrinkage due to Arctic warming reduces red knot fitness in tropical wintering range. *Science* **2016**, *352*, 819–821. [CrossRef]
13. Rakhimberdiev, E.; Duijns, S.; Karagicheva, J.; Camphuysen, C.J.; Dekinga, A.; Dekker, R.; Gavrilov, A.; ten Horn, J.; Jukema, J.; Saveliev, A.; et al. Fuelling conditions at staging sites can mitigate Arctic warming effects in a migratory bird. *Nat. Commun.* **2018**, *9*, 4263. [CrossRef]
14. Salvig, J.C.; Asbirk, S.; Kjeldsen, J.P.; Rasmussen, P.A.F. Wintering waders in the Bijagos Archipelago, Guinee-Bissau 1992–1993. *Ardea* **1994**, *82*, 137–142.
15. Zwarts, L. Numbers and distribution of coastal waders in guinea-bissau. *Ardea* **1988**, *76*, 42–55.
16. Henriques, M.; Belo, J.R.; Sá, J.; Monteiro, H.; Alves, J.A.; Piersma, T.; Dodman, T.; van Roomen, M. The Bijagós Archipelago: A key area for waterbirds of the East Atlantic Flyway. In *East Atlantic Flyway Assessment 2020: The Status of Coastal Waterbird Populations and Their Sites*; van Roomen, M., Citegetse, G., Crowe, O., Dodman, T., Hagemeijer, W., Meise, K., Schekkerman, H., Eds.; Wadden Sea Flyway Initiative: Wilhelmshaven, Germany; Wetlands International: Wageningen, The Netherlands; BirdLife International: Cambridge, UK, 2022; pp. 81–93.
17. Piersma, T. What is Habitat Quality? Dissecting a Research Portfolio on Shorebirds. In *Birds and Habitat: Relationships in Changing Landscapes*; Fuller, R., Ed.; Cambridge University Press: Cambridge, UK, 2012; pp. 383–407.

18. Lourenço, P.M.; Granadeiro, J.P.; Catry, T. Low macroinvertebrate biomass suggests limited food availability for shorebird communities in intertidal areas of the Bijagós archipelago (Guinea-Bissau). *Hydrobiologia* **2018**, *816*, 197–212. [CrossRef]
19. Compton, T.J.; Holthuijsen, S.; Koolhaas, A.; Dekinga, A.; ten Horn, J.; Smith, J.; Galama, Y.; Brugge, M.; van der Wal, D.; van der Meer, J.; et al. Distinctly variable mudscapes: Distribution gradients of intertidal macrofauna across the Dutch Wadden Sea. *J. Sea Res.* **2013**, *82*, 103–116. [CrossRef]
20. Rodrigues, A.M.; Meireles, S.; Pereira, T.; Gama, A.; Quintino, V. Spatial Patterns of Benthic Macroinvertebrates in Intertidal Areas of a Southern European Estuary: The Tagus, Portugal. *Hydrobiologia* **2006**, *555*, 99–113. [CrossRef]
21. Passarelli, C.; Olivier, F.; Paterson, D.M.; Meziane, T.; Hubas, C. Organisms as cooperative ecosystem engineers in intertidal flats. *J. Sea Res.* **2014**, *92*, 92–101. [CrossRef]
22. Umanzor, S.; Ladah, L.; Calderon-Aguilera, L.; Zertuche-González, J. Intertidal macroalgae influence macroinvertebrate distribution across stress scenarios. *Mar. Ecol. Prog. Ser.* **2017**, *584*, 67–77. [CrossRef]
23. Chen, T.Y.; Hwang, G.W.; Mayfield, A.B.; Chen, C.P.; Lin, H.J. The relationship between intertidal soil composition and fiddler crab burrow depth. *Ecol. Eng.* **2017**, *100*, 256–260. [CrossRef]
24. El-Hacen, E.H.M.; Bouma, T.J.; Oomen, P.; Piersma, T.; Olff, H. Large-scale ecosystem engineering by flamingos and fiddler crabs on West-African intertidal flats promote joint food availability. *Oikos* **2019**, *128*, 753–764. [CrossRef]
25. Paulino, J.; Granadeiro, J.P.; Henriques, M.; Belo, J.; Catry, T. Composition and abundance of shorebird and macroinvertebrate communities differ according to densities of burrowing fiddler crabs in tropical intertidal flats. *Hydrobiologia* **2021**, *848*, 3905–3919. [CrossRef]
26. Mathot, K.J.; Piersma, T.; Elner, R.W. Shorebirds as Integrators and Indicators of Mudflat Ecology. In *Mudflat Ecology*; Springer: Cham, Switzerland, 2018; pp. 309–338. [CrossRef]
27. Zhang, C.; Gong, Z.; Qiu, H.; Zhang, Y.; Zhou, D. Mapping typical salt-marsh species in the Yellow River Delta wetland supported by temporal-spatial-spectral multidimensional features. *Sci. Total Environ.* **2021**, *783*, 147061. [CrossRef]
28. Zoffoli, M.L.; Gernez, P.; Rosa, P.; Le Bris, A.; Brando, V.E.; Barillé, A.L.; Harin, N.; Peters, S.; Poser, K.; Spaias, L.; et al. Sentinel-2 remote sensing of Zostera noltei-dominated intertidal seagrass meadows. *Remote Sens. Environ.* **2020**, *251*, 112020. [CrossRef]
29. Pottier, A.; Catry, T.; Trégarot, E.; Maréchal, J.-P.; Fayad, V.; David, G.; Sidi Cheikh, M.; Failler, P. Mapping coastal marine ecosystems of the National Park of Banc d'Arguin (PNBA) in Mauritania using Sentinel-2 imagery. *Int. J. Appl. Earth Obs. Geoinf.* **2021**, *102*, 102419. [CrossRef]
30. Gade, M.; Melchionna, S.; Stelzer, K.; Kohlus, J. Multi-frequency SAR data help improving the monitoring of intertidal flats on the German North Sea coast. *Estuar. Coast. Shelf Sci.* **2014**, *140*, 32–42. [CrossRef]
31. Choi, J.K.; Ryu, J.H.; Lee, Y.K.; Yoo, H.R.; Woo, H.J.; Kim, C.H. Quantitative estimation of intertidal sediment characteristics using remote sensing and GIS. *Estuar. Coast. Shelf Sci.* **2010**, *88*, 125–134. [CrossRef]
32. Wang, W.; Yang, X.; Liu, G.; Zhou, H.; Ma, W.; Yu, Y.; Li, Z. Random forest classification of sediments on exposed intertidal flats using ALOS-2 quad-polarimetric SAR data. *Int. Arch. Photogramm. Remote Sens. Spat. Inf. Sci.* **2016**, *41*, 1191–1194. [CrossRef]
33. Choi, J.K.; Oh, H.J.; Koo, B.J.; Lee, S.; Ryu, J.H. Macrobenthos habitat mapping in a tidal flat using remotely sensed data and a GIS-based probabilistic model. *Mar. Pollut. Bull.* **2011**, *62*, 564–572. [CrossRef]
34. Müller, G.; Stelzer, K.; Smollich, S.; Gade, M.; Adolph, W.; Melchionna, S.; Kemme, L.; Geißler, J.; Millat, G.; Reimers, H.C.; et al. Remotely sensing the German Wadden Sea—A new approach to address national and international environmental legislation. *Environ. Monit. Assess.* **2016**, *188*, 595. [CrossRef]
35. Wade, S.; Hickey, R. Mapping migratory wading bird feeding habitats using satellite imagery and field data, Eighty-Mile Beach, Western Australia. *J. Coast. Res.* **2008**, *24*, 759–770. [CrossRef]
36. Okoye, O.K.; Li, H.; Gong, Z. Retraction of invasive Spartina alterniflora and its effect on the habitat loss of endangered migratory bird species and their decline in YNNR using remote sensing technology. *Ecol. Evol.* **2020**, *10*, 13810–13824. [CrossRef]
37. Jackson, M.V.; Fuller, R.A.; Gan, X.; Li, J.; Mao, D.; Melville, D.S.; Murray, N.J.; Wang, Z.; Choi, C.Y. Dual threat of tidal flat loss and invasive Spartina alterniflora endanger important shorebird habitat in coastal mainland China. *J. Environ. Manage.* **2021**, *278*, 111549. [CrossRef]
38. Danufsky, T.; Colwell, M.A. Winter shorebird communities and tidal flat characteristics at Humboldt Bay, California. *Condor* **2003**, *105*, 117–129. [CrossRef]
39. Morrison, R.I.G. The Use of Remote Sensing to Evaluate Shorebird Habitats and Populations on Prince Charles Island, Foxe Basin, Canada. *Arctic* **1997**, *50*, 55–75. [CrossRef]
40. Zhang, T.; Tian, B.; Bo, S.; Yuan, L.; Zhao, Y.; Yuan, X. Mapping the conservation priority of migratory shorebird habitat on a dynamic deltaic coast. *Estuar. Coast. Shelf Sci.* **2018**, *212*, 219–232. [CrossRef]
41. Schulte to Bühne, H.; Pettorelli, N. Better together: Integrating and fusing multispectral and radar satellite imagery to inform biodiversity monitoring, ecological research and conservation science. *Methods Ecol. Evol.* **2018**, *9*, 849–865. [CrossRef]
42. ESA. The European Space Agency. Available online: https://sentinels.copernicus.eu/ (accessed on 12 December 2021).
43. Jung, R.; Adolph, W.; Ehlers, M.; Farke, H. A multi-sensor approach for detecting the different land covers of tidal flats in the German Wadden Sea—A case study at Norderney. *Remote Sens. Environ.* **2015**, *170*, 188–202. [CrossRef]
44. Gade, M.; Wang, W.; Kemme, L. On the imaging of exposed intertidal flats by single- and dual-co-polarization Synthetic Aperture Radar. *Remote Sens. Environ.* **2018**, *205*, 315–328. [CrossRef]
45. Breiman, L. Random Forests. *Mach. Learn.* **2001**, *45*, 5–32. [CrossRef]

46. Belgiu, M.; Drăgu, L. Random forest in remote sensing: A review of applications and future directions. *ISPRS J. Photogramm. Remote Sens.* **2016**, *114*, 24–31. [CrossRef]
47. Khatami, R.; Mountrakis, G.; Stehman, S.V. A meta-analysis of remote sensing research on supervised pixel-based land-cover image classification processes: General guidelines for practitioners and future research. *Remote Sens. Environ.* **2016**, *177*, 89–100. [CrossRef]
48. Zhang, F.; Yang, X. Improving land cover classification in an urbanized coastal area by random forests: The role of variable selection. *Remote Sens. Environ.* **2020**, *251*, 112105. [CrossRef]
49. Campredon, P.; Catry, P. Bijagos Archipelago (Guinea-Bissau). In *The Wetland Book. II: Distribution, Description, and Conservation*; Finlayson, C.M., Milton, G.R., Prentice, R.C., Davidson, N.C., Eds.; Springer: Dordrecht, The Netherlands, 2017; pp. 1333–1340. ISBN 9789400740006.
50. Cuq, F.; Campredon, P.; Giraudet, J.; Giraudet, E.; Gourmelon, F.; Pennober, G.; Simão da Silva, A. *Un Système D'information Géographique Pour L'aide à la Gestion Intégrée de L'archipel des Bijagos (Guinée-Bissau): Notice de la Carte, Constitution et Exploitation du SIG*; Laboratoire Géosystèmes: Brest, France, 2001; ISBN 2-9516590-0-8.
51. Pennober, G. Analyse Spatiale de L'environnement Côtier de L'archipel des Bijagos (Guinée Bissau). Ph.D. Thesis, Université de Bretagne Occidentale, Brest, France, 1999.
52. Temudo, M.P.; Cabral, A.I. The Social Dynamics of Mangrove Forests in Guinea-Bissau, West Africa. *Hum. Ecol.* **2017**, *45*, 307–320. [CrossRef]
53. Pennober, G. *Dynamique Littorale d'un Delta Estuarien: Les Bijagos (Guinée-Bissau)*; Institut de Géographie et D'aménagement Régional: Nantes, France, 2003.
54. Granadeiro, J.P.; Andrade, J.; Palmeirim, J.M. Modelling the distribution of shorebirds in estuarine areas using generalised additive models. *J. Sea Res.* **2004**, *52*, 227–240. [CrossRef]
55. Ponsero, A.; Sturbois, A.; Desroy, N.; Le Mao, P.; Jones, A.; Fournier, J. How do macrobenthic resources concentrate foraging waders in large megatidal sandflats? *Estuar. Coast. Shelf Sci.* **2016**, *178*, 120–128. [CrossRef]
56. Finn, P.G.; Catterall, C.P.; Driscoll, P.V. Prey versus substrate as determinants of habitat choice in a feeding shorebird. *Estuar. Coast. Shelf Sci.* **2008**, *80*, 381–390. [CrossRef]
57. Lourenço, P.M.; Catry, P.; Lecoq, M.; Ramírez, I.; Granadeiro, J.P. Role of disturbance, geology and other environmental factors in determining abundance and diversity in coastal avian communities during winter. *Mar. Ecol. Prog. Ser.* **2013**, *479*, 223–234. [CrossRef]
58. Green, L.; Blumstein, D.T.; Fong, P. Macroalgal Mats in a Eutrophic Estuary Obscure Visual Foraging Cues and Increase Variability in Prey Availability for Some Shorebirds. *Estuaries and Coasts* **2015**, *38*, 917–926. [CrossRef]
59. Besterman, A.F.; Karpanty, S.M.; Pace, M.L. Impact of exotic macroalga on shorebirds varies with foraging specialization and spatial scale. *PLoS ONE* **2020**, *15*, e0231337. [CrossRef]
60. Everett, R.A. Macroalgae in marine soft-sediment communities: Effects on benthic faunal assemblages. *J. Exp. Mar. Bio. Ecol.* **1994**, *175*, 253–274. [CrossRef]
61. Somerfield, P.J.; McClelland, I.L.; McNeill, C.L.; Bolam, S.G.; Widdicombe, S. Environmental and sediment conditions, infaunal benthic communities and biodiversity in the Celtic Sea. *Cont. Shelf Res.* **2019**, *185*, 23–30. [CrossRef]
62. Philippe, A.S.; Pinaud, D.; Cayatte, M.L.; Goulevant, C.; Lachaussée, N.; Pineau, P.; Karpytchev, M.; Bocher, P. Influence of environmental gradients on the distribution of benthic resources available for shorebirds on intertidal mudflats of Yves Bay, France. *Estuar. Coast. Shelf Sci.* **2016**, *174*, 71–81. [CrossRef]
63. Folk, R.L.; Andrews, P.B.; Lewis, D.W. Detrital sedimentary rock classification and nomenclature for use in new zealand. *New Zeal. J. Geol. Geophys.* **1970**, *13*, 937–968. [CrossRef]
64. ESA. *Sentinel-2 User Handbook*; European Space Agency: Paris, France, 2015.
65. Richter, R.; Schläpfer, D. *Atmospheric/Topographic Correction for Satellite Imagery*; ReSe Applications Schlapfer: Wil, Switzerland, 2012; ISBN 9788578110796.
66. Filipponi, F. Sentinel-1 GRD Preprocessing Workflow. *Proceedings* **2019**, *18*, 11. [CrossRef]
67. Medasani, S.; Reddy, G.U. Analysis and Evaluation of Speckle Filters by Using Polarimetric Synthetic Aperture Radar Data Through Local Statistics. In Proceedings of the 2018 Second International Conference on Electronics, Communication and Aerospace Technology (ICECA), Coimbatore, India, 29–31 March 2018; pp. 169–174. [CrossRef]
68. Abramov, S.; Rubel, O.; Lukin, V.; Kozhemiakin, R.; Kussul, N.; Shelestov, A.; Lavreniuk, M. Speckle reducing for Sentinel-1 SAR data. In Proceedings of the International Geoscience and Remote Sensing Symposium (IGARSS), Fort Worth, TX, USA, 23–28 July 2017; Institute of Electrical and Electronics Engineers Inc.: Piscataway, NJ, USA, 2017; Volume 2017, pp. 2353–2356.
69. Granadeiro, J.P.; Belo, J.; Henriques, M.; Catalão, J.; Catry, T. Using Sentinel-2 images to estimate topography, tidal-stage lags and exposure periods over large intertidal areas. *Remote Sens.* **2021**, *13*, 320. [CrossRef]
70. Legendre, P. *Lmodel2: Model II Regression*; R Package: Vienna, Austria, 2018.
71. Catalão, J. Uma nova técnica para determinar a batimetria intertidal com imagens multiespectrais do satélite Sentinel-2. In *Actas das 5.as Jornadas de Engenharia Hidrog*; Instituto Hidrográfico: Lisbon, Portugal, 2018; pp. 19–22.
72. Bué, I.; Catalão, J.; Semedo, Á. Intertidal bathymetry extraction with multispectral images: A logistic regression approach. *Remote Sens.* **2020**, *12*, 1311. [CrossRef]

73. McFeeters, S.K. The use of the Normalized Difference Water Index (NDWI) in the delineation of open water features. *Int. J. Remote Sens.* **1996**, *17*, 1425–1432. [CrossRef]
74. Wood, S.N. *Generalized Additive Models*, 2nd ed.; Chapman and Hall/CRC: Boca Raton, FL, USA, 2017; ISBN 9781315370279.
75. Commo, F.; Bot, B.M. Package nplr: N-Parameter Logistic Regression. 2016. Available online: https://mran.revolutionanalytics.com/snapshot/2015-07-13/web/packages/nplr/vignettes/nplr.pdf (accessed on 16 May 2022).
76. Xu, H. Modification of normalised difference water index (NDWI) to enhance open water features in remotely sensed imagery. *Int. J. Remote Sens.* **2006**, *27*, 3025–3033. [CrossRef]
77. Wilson, E.H.; Sader, S.A. Detection of forest harvest type using multiple dates of Landsat TM imagery. *Remote Sens. Environ.* **2002**, *80*, 385–396. [CrossRef]
78. Xiao, X.; Boles, S.; Liu, J.; Zhuang, D.; Frolking, S.; Li, C.; Salas, W.; Moore, B. Mapping paddy rice agriculture in southern China using multi-temporal MODIS images. *Remote Sens. Environ.* **2005**, *95*, 480–492. [CrossRef]
79. Tucker, C.J. Red and photographic infrared linear combinations for monitoring vegetation. *Remote Sens. Environ.* **1979**, *8*, 127–150. [CrossRef]
80. Qi, J.; Kerr, Y.; Chehbouni, A. External factor consideration in vegetation index development. In Proceedings of the International Symposium on Physical Measurements and Signatures in Remote Sensing, Val-d'isere, France, 17–22 January 1994.
81. Qi, J.; Chehbouni, A.; Huete, A.R.; Kerr, Y.H.; Sorooshian, S. A modified soil adjusted vegetation index. *Remote Sens. Environ.* **1994**, *48*, 119–126. [CrossRef]
82. Xiao, C.; Li, P.; Feng, Z.; Liu, Y.; Zhang, X. Sentinel-2 red-edge spectral indices (RESI) suitability for mapping rubber boom in Luang Namtha Province, northern Lao PDR. *Int. J. Appl. Earth Obs. Geoinf.* **2020**, *93*, 102176. [CrossRef]
83. Chen, W.; Liu, L.; Zhang, C.; Wang, J.; Wang, J.; Pan, Y. Monitoring the seasonal bare soil areas in Beijing using multi-temporal TM images. *Int. Geosci. Remote Sens. Symp.* **2004**, *5*, 3379–3382. [CrossRef]
84. Xiao, J.; Shen, Y.; Tateishi, R.; Bayaer, W. Development of topsoil grain size index for monitoring desertification in arid land using remote sensing. *Int. J. Remote Sens.* **2006**, *27*, 2411–2422. [CrossRef]
85. Tuszynski, J. caTools: Moving Window Statistics, GIF, Base64, ROC AUC, etc. R package version 1. 2021.
86. Liaw, A.; Wiener, M. Package 'randomForest': Breiman and Cutler's Random Forests for Classification and Regression. R package version 4. 2018.
87. Gregorutti, B.; Michel, B.; Saint-Pierre, P. Correlation and variable importance in random forests. *Stat. Comput.* **2017**, *27*, 659–678. [CrossRef]
88. Pelletier, C.; Valero, S.; Inglada, J.; Champion, N.; Dedieu, G. Assessing the robustness of Random Forests to map land cover with high resolution satellite image time series over large areas. *Remote Sens. Environ.* **2016**, *187*, 156–168. [CrossRef]
89. Speiser, J.L.; Miller, M.E.; Tooze, J.; Ip, E. A comparison of random forest variable selection methods for classification prediction modeling. *Expert Syst. Appl.* **2019**, *134*, 93–101. [CrossRef] [PubMed]
90. Lunetta, K.L.; Hayward, L.B.; Segal, J.; van Eerdewegh, P. Screening large-scale association study data: Exploiting interactions using random forests. *BMC Genet.* **2004**, *5*, 32. [CrossRef]
91. Diaz-Uriarte, R. GeneSrF and varSelRF: A web-based tool and R package for gene selection and classification using random forest. *BMC Bioinform.* **2007**, *8*, 328. [CrossRef]
92. Genuer, R.; Poggi, J.M.; Tuleau-Malot, C. VSURF: An R package for variable selection using random forests. *R J.* **2015**, *7*, 19–33. [CrossRef]
93. Conrad, O.; Bechtel, B.; Bock, M.; Dietrich, H.; Fischer, E.; Gerlitz, L.; Wehberg, J.; Wichmann, V.; Böhner, J. System for Automated Geoscientific Analyses (SAGA) v. 2.1.4. *Geosci. Model Dev.* **2015**, *8*, 1991–2007. [CrossRef]
94. Lu, Q.; Huang, X.; Liu, T.; Zhang, L. A structural similarity-based label-smoothing algorithm for the post-processing of land-cover classification. *Remote Sens. Lett.* **2016**, *7*, 437–445. [CrossRef]
95. Zhu, X. Land cover classification using moderate resolution satellite imagery and random forests with post-hoc smoothing. *J. Spat. Sci.* **2013**, *58*, 323–337. [CrossRef]
96. Huang, X.; Lu, Q.; Zhang, L.; Plaza, A. New postprocessing methods for remote sensing image classification: A systematic study. *IEEE Trans. Geosci. Remote Sens.* **2014**, *52*, 7140–7159. [CrossRef]
97. Schindler, K. An overview and comparison of smooth labeling methods for land-cover classification. *IEEE Trans. Geosci. Remote Sens.* **2012**, *50*, 4534–4545. [CrossRef]
98. Kuhn, M. Caret Package. *J. Stat. Softw.* **2008**, *28*, 1–26.
99. Velez, D.R.; White, B.C.; Motsinger, A.A.; Bush, W.S.; Ritchie, M.D.; Williams, S.M.; Moore, J.H. A balanced accuracy function for epistasis modeling in imbalanced datasets using multifactor dimensionality reduction. *Genet. Epidemiol.* **2007**, *31*, 306–315. [CrossRef] [PubMed]
100. Wegmann, M.; Leutner, B.; Dech, S. *Remote Sensing and GIS for Ecologists: Using Open Source Software*; Wegmann, M., Leutner, B., Dech, S., Eds.; Pelagic Publishing: Exeter, UK, 2016; ISBN 978-1-78427-028-5.
101. Stehman, S.V. Selecting and interpreting measures of thematic classification accuracy. *Remote Sens. Environ.* **1997**, *62*, 77–89. [CrossRef]
102. Congalton, R.G. A review of assessing the accuracy of classifications of remotely sensed data. *Remote Sens. Environ.* **1991**, *37*, 35–46. [CrossRef]

103. Kim, K.L.; Kim, B.J.; Lee, Y.K.; Ryu, J.H. Generation of a large-scale surface sediment classification map using unmanned aerial vehicle (UAV) data: A case study at the Hwang-do tidal flat, Korea. *Remote Sens.* **2019**, *11*, 229. [CrossRef]
104. Adolph, W.; Farke, H.; Lehner, S.; Ehlers, M. Remote sensing intertidal flats with TerraSAR-X. A SAR perspective of the structural elements of a tidal basin for monitoring the Wadden Sea. *Remote Sens.* **2018**, *10*, 1085. [CrossRef]
105. Kohlus, J.; Stelzer, K.; Müller, G.; Smollich, S. Mapping seagrass (Zostera) by remote sensing in the Schleswig-Holstein Wadden Sea. *Estuar. Coast. Shelf Sci.* **2020**, *238*, 106699. [CrossRef]
106. Fitton, J.M.; Rennie, A.F.; Hansom, J.D.; Muir, F.M.E. Remotely sensed mapping of the intertidal zone: A Sentinel-2 and Google Earth Engine methodology. *Remote Sens. Appl. Soc. Environ.* **2021**, *22*, 100499. [CrossRef]
107. Bousbih, S.; Zribi, M.; Pelletier, C.; Gorrab, A.; Lili-Chabaane, Z.; Baghdadi, N.; Aissa, N.B.; Mougenot, B. Soil texture estimation using radar and optical data from Sentinel-1 and Sentinel-2. *Remote Sens.* **2019**, *11*, 1520. [CrossRef]
108. Ibrahim, E.; Adam, S.; De Wever, A.; Govaerts, A.; Vervoort, A.; Monbaliu, J. Investigating spatial resolutions of imagery for intertidal sediment characterization using geostatistics. *Cont. Shelf Res.* **2014**, *85*, 117–125. [CrossRef]
109. Wang, W.; Yang, X.; Li, X.; Chen, K.; Liu, G.; Li, Z.; Gade, M. A Fully Polarimetric SAR Imagery Classification Scheme for Mud and Sand Flats in Intertidal Zones. *IEEE Trans. Geosci. Remote Sens.* **2017**, *55*, 1734–1742. [CrossRef]
110. Deroin, J.P. Combining ALOS and ERS-2 SAR data for the characterization of tidal flats. Case study from the Baie des Veys, Normandy, France. *Int. J. Appl. Earth Obs. Geoinf.* **2012**, *18*, 183–194. [CrossRef]
111. Wang, X.; Xiao, X.; Zou, Z.; Chen, B.; Ma, J.; Dong, J.; Doughty, R.B.; Zhong, Q.; Qin, Y.; Dai, S.; et al. Tracking annual changes of coastal tidal flats in China during 1986–2016 through analyses of Landsat images with Google Earth Engine. *Remote Sens. Environ.* **2020**, *238*, 110987. [CrossRef]
112. Ryu, J.H.; Na, Y.H.; Won, J.S.; Doerffer, R. A critical grain size for Landsat ETM+ investigations into intertidal sediments: A case study of the Gomso tidal flats, Korea. *Estuar. Coast. Shelf Sci.* **2004**, *60*, 491–502. [CrossRef]
113. Choi, J.K.; Eom, J.A.; Ryu, J.H. Spatial relationships between surface sedimentary facies distribution and topography using remotely sensed data: Example from the Ganghwa tidal flat, Korea. *Mar. Geol.* **2011**, *280*, 205–211. [CrossRef]
114. Instituto Hidrográfico. Vol II Países Africanos de Língua Oficial Portuguesa e Macau. In *Tabelas de Marés*; Instituto Hidrográfico: Lisboa, Portugal, 2021.
115. Hill, N.K.; Woodworth, B.K.; Phinn, S.R.; Murray, N.J.; Fuller, R.A. Global protected-area coverage and human pressure on tidal flats. *Conserv. Biol.* **2021**, *35*, 933–943. [CrossRef]
116. Zwarts, L. The winter exploitation of Fiddler Crabs Uca tangeri by waders in Guinea-Bissau. *Ardea* **1985**, *73*, 3–12.
117. *East Atlantic Flyway Assessment 2020: The Status of Coastal Waterbird Populations and Their Sites*; Van Roomen, M.; Citegetse, G.; Crowe, O.; Dodman, T.; Hagemeijer, W.; Meise, K.; Schekkerman, H. (Eds.) Wadden Sea Flyway Initiative: Wilhelmshaven, Germany; Wetlands International: Wageningen, The Netherlands; BirdLife International: Cambridge, UK, 2022.